

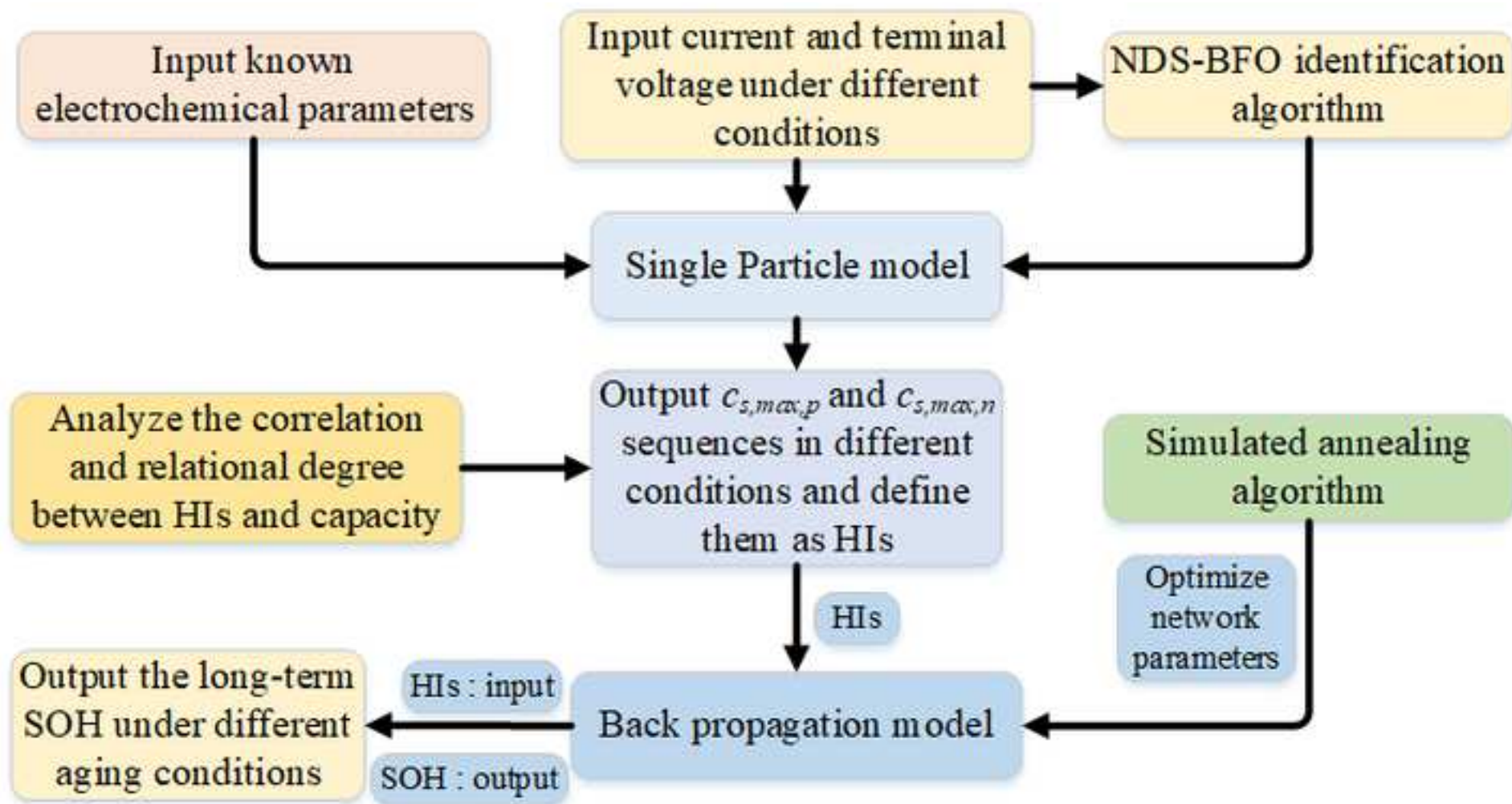
XIONG, R., WANG, S., YU, C., FERNANDEZ, C., XIAO, W. and JIA, J. 2023. A novel nonlinear decreasing step-bacterial foraging optimization algorithm and simulated annealing-back propagation model for long-term battery state of health estimation. *Journal of energy storage* [online], 59, article 106484. Available from: <https://doi.org/10.1016/j.est.2022.106484>

# A novel nonlinear decreasing step-bacterial foraging optimization algorithm and simulated annealing-back propagation model for long-term battery state of health estimation.

XIONG, R., WANG, S., YU, C., FERNANDEZ, C., XIAO, W. and JIA, J.

2023

© 2022 Elsevier Ltd.



# A Novel Nonlinear Decreasing Step-Bacterial Foraging Optimization Algorithm and Simulated Annealing-Back Propagation Model for Long-term Battery State of Health Estimation

Ran Xiong<sup>1,2,3</sup>, Shunli Wang<sup>1,2,\*</sup>, Chunmei Yu<sup>1</sup>, Carlos Fernandez<sup>4</sup>, Wei Xiao<sup>3</sup>, Jun Jia<sup>3</sup>

<sup>1</sup>*School of Information Engineering, Southwest University of Science and Technology, Mianyang, 621010,*

*China;*

<sup>2</sup>*College of Electrical Engineering, Sichuan University, Chengdu, 610065, China;*

<sup>3</sup>*Sichuan Energy Internet Research Institute, Tsinghua University, Chengdu, 610042, China;*

<sup>4</sup>*School of Pharmacy and Life Sciences, Robert Gordon University, Aberdeen, AB10-7GJ, UK.*

**Abstract:** With the rapid development of electric energy storage, more and more attention has been paid to the accurate construction of energy storage lithium-ion battery (LIB) model and the efficient monitoring of battery states. Based on this requirement, a simulated annealing-back propagation (SA-BP) model is proposed, and the long-term state of health (SOH) of LIBs can be estimated online by combining with the battery single particle (SP) model. Among them, simulated annealing (SA) algorithm is used to optimize the initial parameters of back propagation (BP) network. In order to improve the identification efficiency and avoid the local optimization, the nonlinear decreasing step-bacterial foraging optimization (NDS-BFO) algorithm is introduced into the parameter identification process. On the basis of adopting the SOH sequence as the output of the SA-BP model, two electrochemical parameter sequences are used as the input of the model for training and testing. In addition, in this paper, the contributions in terms of the SOH estimation task mainly include two aspects. Firstly, the SOH estimation results can provide suggestions for the timely replacement of batteries in actual energy storage power stations. Secondly, the electrochemical parameters identified before SOH estimation are strongly related to the quality of the LIB. Therefore, they can provide references for the economy of LIBs. At 25 °C, the accuracy of the SP model is verified under three different working conditions. Degradation experiments are carried out under a constant current condition and a self-designed energy storage condition. The experimental results show that, under the 0.5 rate constant current condition, the root mean square error (RMSE), mean absolute error (MAE) and mean absolute percentage error (MAPE) of the long-term

SOH estimation result are 0.42%, 0.34% and 0.38, respectively. And under the self-designed energy storage condition, the RMSE, MAE and MAPE of the result are 0.33%, 0.26% and 0.29, respectively. Under the same working condition, the SOH estimation results have a significant improvement in various performance evaluation indicators. The improved algorithm provides theoretical and experimental basis for the reliability of energy storage battery monitoring.

**Key words:** simulated annealing-back propagation model; nonlinear decreasing step-bacterial foraging optimization algorithm; lithium-ion battery; state of health; single particle model

\***Corresponding author:** Shun-Li Wang. Tel: +86-15884655563. E-mail address: 497420789@qq.com.

## 1. Introduction

Energy storage is an important technology for building new power systems, and it can support to achieve carbon peaking and carbon neutrality. The traditional energy storage mainly includes mechanical energy storage and electrochemical energy storage [1, 2]. In energy storage power stations, electrochemical energy storage technology has become the main support [3, 4]. Among them, electrochemical energy storage devices represented by LIBs have been widely used in new power systems, and the common type of energy storage LIB is lithium iron phosphate battery [1, 3, 4]. With the advantages of long cycle life and good rate performance, the lithium iron phosphate battery plays an irreplaceable role in power system [5-8]. In the process of degradation, the internal resistance of each LIB will gradually increase. The increase of internal resistance is one of the inducements to increase the risk of thermal runaway. If LIBs are not properly managed during the degradation process, a series of thermal runaway problems may be caused. In the past decade, there have been dozens of fire and explosion accidents caused by thermal runaway [4, 9]. Therefore, the establishment of the safe and stable battery management system (BMS) is the focus and difficulty of energy storage systems [10, 11].

The efficient operation of energy storage system components is mainly determined by the states of LIBs [12]. During the degradation process, accurate and online monitoring of long-term SOH can ensure that the battery is within a safe working range. And the SOH can provide effective references for the screening of abnormal cell [13, 14]. From the technical point of view, the SOH is a key indicator reflecting battery performance, and it can be used as a reference for optimizing energy

management strategies [15-17]. From the economic point of view, the battery wear cost is closely related to the number of degradation cycles. Therefore, the SOH can be used as a reference for judging battery economy [18]. The definition of cell SOH includes capacity definition method and internal resistance definition method [19-23]. The capacity definition method defines SOH as the ratio of current capacity to initial capacity, and the internal resistance definition method defines SOH as the ratio of internal resistance difference. Among the internal resistance definition method, the denominator is the internal resistance difference between the end state and the initial state, and the numerator is the internal resistance difference between the end state and the current state. In electric vehicles, the change of SOH is characterized by the increase of internal resistance. In this case, the SOH reflects energy capability. In electrochemical energy storage systems, the change of SOH is characterized by capacity degradation. In this case, the SOH reflects power capability [24]. In addition, some scholars have given the definition of other cell SOH. For example, the SOH can be quantified by monitoring the recyclable lithium ions or solid-phase diffusion time of positive lithium ions [25, 26]. Due to the nonlinear and complex characteristics of LIBs, the effective estimation of SOH in the energy storage system is a great challenge.

In recent years, the estimation algorithms of SOH include direct measurement method and indirect analysis method. On the one hand, SOH is directly obtained through instruments and experiments. Direct measurement method mainly includes Coulomb counting method and electrochemical impedance spectroscopy (EIS) method [27]. The core idea of Coulomb counting method is to calculate SOH through current integral and SOC difference under a complete constant current discharge condition. However, because the method strongly depends on the SOC difference and current integral, the measurement error will gradually accumulate [15, 28]. The EIS method obtains the charge transfer resistance and SEI film resistance inside LIBs through the excitation voltage and response current [23, 29]. And some researchers believe that the above-mentioned resistances have the potential to estimate SOH [30]. Although the EIS method has high accuracy in obtaining SOH, the related tests are complex [31, 32]. In addition, the direct measurement method also includes internal resistance measurement method [33], cycle count method [34] and destructive test method [35]. However, all the above-mentioned direct measurement methods cannot be applied to complex energy storage systems.

On the other hand, the indirect analysis method is to estimate SOH indirectly through relevant parameters. This method has gradually become a research hotspot in recent years due to its own advantages. The indirect analysis method includes data-driven method, physical model-based method and hybrid model-based method. Among them, the data-driven method does not establish a meaningful model, but extracts information related to the SOH for relevant calculation. Data-driven method for SOH estimation can be divided into two categories: machine learning-based (ML-based) method and differential analysis-based (DA-based) method. The ML-based method estimates SOH by extracting useful information and using ML technology [36]. Among them, the extracted feature data is called health indicators (HIs). In practical research, HIs should be highly correlated with SOH. How to select appropriate HIs is the key to estimate SOH in ML-based method. The core idea of ML method is to construct corresponding model through data learning and identification.

ML-based method includes artificial neural network (ANN), support vector machine (SVM) and relevant vector machine (RVM). ANN can simulate brain behavior and has strong nonlinear mapping ability [37-39]. Various recent papers have divided ANN method into traditional ANN method and DL method. And they have been widely used in estimating SOH of LIBs [40]. Traditional ANN generally refers to feedforward neural network (FFNN) [41], while deep learning (DL) includes recurrent neural network (RNN) [42], deep neural network (DNN) [43] and convolutional neural network (CNN) [44]. For the FFNN, Pan et al. used the terminal voltage during constant current charging as the input of FFNN to estimate the SOH of LIBs [45]. The RNN includes Elman neural network (ENN) and long short-term memory (LSTM). For the ENN, Chen et al. extracted HIs related to battery degradation [46]. And the HIs were used as the input of ENN model to estimate SOH. For the LSTM, Lee et al. estimated SOH by establishing a multi-layer LSTM neural network model [47]. Besides, the LSTM model are divided into normal, caution and fault based on SOH estimation results. For the CNN, Shen et al. proposed a cell-level online SOH estimation method for LIBs based on deep convolution neural network (DCNN) and operating parameters [48]. It is worth noting that in this literature, the inputs of SOH estimation model are directly measurable data, including voltage, current and charging capacity. Therefore, the SOH estimation method proposed in this literature belongs to a DL-based end-to-end method. For the DNN, Lee et al. developed a DNN model suitable for high temperature conditions to

estimate SOH based on the discharge voltage data [49]. The core idea of SVM is to find some support vectors that can describe the system [50]. On this basis, the nonlinear model can be transformed into a linear model by using regression algorithm. In the field of SOH estimation, Nuhic et al. optimized a SVM model by considering the change of temperature, SOC and charge-discharge rate [51]. In addition, Liu et al. established a model based on indirectly enhanced HIs and support vector regression [52]. The basic idea of RVM is similar to that of SVM, but RVM adopts a probability-based approach. From the perspective of optimizing the relevant vectors and improving the HIs, Wang et al. [53] and Li et al. [54] constructed two novel RVM models for SOH estimation, respectively.

The core idea of the DA-based method is to obtain the characteristics related to SOH degradation from the differentiated curves of LIBs. In recent years, DA-based methods such as incremental capacity analysis (ICA) method and differential voltage analysis (DVA) method have been widely used in the research of battery degradation mechanism and estimation of SOH [55]. The ICA method and the DVA method estimate the SOH by extracting features such as peak value, amplitude, and envelope area of the curve [56]. For example, based on incremental voltage difference, Naha et al. indicated a SOH estimation method by introducing a feature vector composed of the difference between voltage and temperature [57]. Compared with ML-based method, DA-based method can directly reflect the degradation of LIBs from the differentiated curves. However, DA-based method highly depends on the complete low-rate constant current condition. Therefore, this method is not suitable for actual energy storage conditions.

Physical model-based SOH estimation method includes equivalent circuit model-based (ECM-based) method and electrochemical model-based (EM-based) methods. ECMs have clear physical meaning and simple mathematical expressions [58]. In addition to the common Rint model, Thevenin model, second-order RC model, PNGV model and GNL model, there are many forms of ECMs [59]. For example, based on the second-order RC model, Zeng et al. established an improved second-order RC model by adding high capacitance and current-controlled current source [60]. On the basis of Thevenin model and open-circuit voltage lag characteristics, He et al. proposed an equivalent hysteresis model with variable parameters [61]. Hu et al. compared the evaluation indexes of 12 ECMs under different conditions and temperatures, and

believed that the first-order RC model with hysteresis effect is most suitable for lithium iron phosphate battery [62]. After establishing the ECM model, it is necessary to identify the model parameters. ECM parameter identification methods include curve method of fitting comparison and least square (LS) method [63]. In the curve method of fitting comparison, the pulse current test is indispensable. Therefore, it can only be used for offline identification. The LS method continuously updates the model parameters according to the error between the model output and the actual output to obtain the optimal solution [64]. Rijanto et al. [65] and Shi et al. [66] adopted two different RLS algorithms to identify ECM parameters. After parameter identification, filtering algorithm is needed to estimate SOH. The state space model is established by constructing the state equation. And the SOH is solved dynamically and iteratively by using the filtering algorithm. At present, common filtering algorithms include Kalman filtering and particle filtering [67, 68]. For example, Ling et al. proposed a co-estimation method of state of charge (SOC) and SOH by combining fractional second-order RC model and double extended Kalman filtering algorithm [69]. Based on the fractional second-order RC model, Ma et al. used a multi-innovations unscented Kalman filter and a unscented Kalman filter for co-estimation of SOC and SOH [70]. Bi et al. developed a SOH estimation method based on second-order RC battery pack ECM and genetic resampling particle filtering algorithm [71].

At present, the common EMs used to estimate battery states include pseudo-two-dimensional (P2D) model and its simplified models. Among them, the P2D model is difficult to be applied to practical engineering because of its complex calculation. The simplification methods of the P2D model are mainly divided into two types. The first simplification method is to reduce the order and expression of the formula from a mathematical point of view. For example, Deng et al. reduced the P2D model by using the principle of polynomial approximation [72]. Lee et al. used the discrete-time realization algorithm to reduce the order of five partial differential equations describing the porous electrode theory [73]. Another simplification method is to simplify the structure or parameters of the model. Among them, the SP model is the most representative. The SP model is an EM with the most simplified parameters and structure [74]. Compared with the P2D model, the calculation process of the SP model is simplified, but the simulation effect is poor at high rates. Based on the SP model, a series of improved models are developed. For example, by considering the influence of electrolyte on output voltage, Grandjean et al.

developed a SP model with electrolyte [75]. Besides, Mehta et al. proposed an extended SP model by considering the spatial variation of overpotential and open-circuit potential [76]. In addition, there are other simplified models such as electrode averaged model based on kinetic reaction [77]. Similarly, after the appropriate EM is established, the method based on the EM also needs to identify the model parameters. Due to the complexity and diversity of EM parameters, the commonly used parameter identification method is multi-objective optimization algorithm. For example, Wu et al. identified the maximum solid-phase lithium-ion concentration of positive and negative electrodes through linear decreasing weight-particle swarm optimization algorithm [78]. Moura et al. developed an adaptive partial differential equation observer to obtain the internal resistance and the number of recyclable lithium ions [79]. After identifying the electrochemical parameters, it is also necessary to combine the filtering method for SOH estimation. When the filtering method based on EM is used to estimate the SOH, the capacity or internal resistance is selected as the state variable. Zheng et al., Zou et al. and Bartlett et al. estimated the internal resistance or capacity to obtain the SOH through proportional integral observer, multi time scale observer, and extend Kalman filter-particle filter, respectively.

Data-driven methods do not require establishing any meaningful models, but they are strongly dependent on the selection of HIs and training methods. Besides, the ECM-based methods have low estimation accuracy, and the EM-based methods are complex. Therefore, the hybrid model-based method has become a hot topic in related research fields during recent years. The hybrid model-based method is divided into five types: direct measurement combined with physical model-based method, direct measurement combined with data-driven method, data-driven combined with physical model-based method, different physical model-based methods combined, and different data-driven methods combined. For the first type, Xiong et al. estimated SOH based on EIS and dual polarization model [80]. For the second type, Zenati et al. proposed a method based on EIS and fuzzy logic to estimate SOH [81]. For the third type, Che et al. [82] and Park et al. [83] believed that SOH can be estimated by combining ECMs and data-driven methods. Che et al. used an ECM and a nonlinear autoregressive neural network with exogenic input to estimate SOH. Park et al. developed a SOH estimation method based on Thevenin ECM and multivariate autoregression model. For the fourth type, Chu et al. established a model to estimate SOH by combining the

electrochemical mechanism and the ECM with constant phase element [84]. For the last type, Chen et al. developed a SOH estimation method based on autoregressive moving average model and ENN. Besides, Fan et al. developed a deep learning-based end-to-end SOH estimation method [85]. In this method, the directly observed voltage and current are taken as the input of the gate recurrent unit-convolutional neural network (GRU-CNN), and the SOH is taken as the output of the network. Kaur et al. studied three end-to-end SOH estimation methods from FFNN, CNN and LSTM [86]. And the superiority of LSTM-based end-to-end SOH estimation method is verified. The end-to-end SOH estimation method omitted the extraction of HIs in the learning process [87]. Manual extraction of HIs is expensive. Correspondingly, if the extracted HIs are important for battery analysis, it is not suitable to use the end-to-end model. The basis of using deep learning-based end-to-end model for SOH estimation is sufficient training data [88]. Under the premise of sufficient data and no need for HIs, the deep learning-based end-to-end model has broad prospects.

In this paper, a novel hybrid model-based SOH estimation method is proposed. Firstly, the SP model is established, and the NDS-BFO algorithm is used to identify the maximum solid-phase lithium-ion concentration of positive and negative electrodes during degradation process. Using the above parameters as HIs can improve the versatility of the NN model. Secondly, the high correlation between the parameters and the capacity is analyzed. Finally, under the self-designed working conditions, the HIs are used as the input of SA-BP model to estimate the long-term SOH of energy storage LIBs. The experimental results show that, compared with the algorithm before the improvement, the results of the proposed algorithm have obvious advantages in various performance evaluation indicators. Moreover, compared with some existing ML-based SOH estimation methods, the proposed algorithm demonstrates better performance on multiple indicators.

The clear motivation for proposing this novel algorithm includes two parts. Firstly, the estimation results of SOH can provide references for updating the cells in the energy storage power station. When the SOH difference between one cell and other cells is too large, it is necessary to replace this cell for avoiding the overall performance degradation. Secondly, the model applicable to various working conditions can improve the efficiency of SOH estimation. At present, common

estimation models can only be applied to a single working condition. To solve this problem, this paper extracts HIs that can be applied to a variety of working conditions. And the HIs are taken as the input of SOH estimation model.

Furthermore, the work of this paper has the following novelties or superiorities with respect to other relevant work. Firstly, the proposed SOH estimation method is relatively long-term compared with the co-estimation method of SOC and SOH. Common co-estimation methods of SOC and SOH only concern about the SOH change in a charge-discharge cycle. And this is of little significance for the continuously degradation LIBs in the energy storage power station. Secondly, this paper establishes a non-end-to-end neural network that needs to extract HIs. The premise of using end-to-end neural network model is massive training data. For this paper, the data used for model training is not enough to support the end-to-end model. The extracted HIs are the maximum solid-phase lithium-ion concentration of positive and negative electrodes. And they are of great significance for exploring the piezo-electro-chemical coupling mechanism, optimizing the existing commercial electrode design, and improving the battery performance. Among them, the piezo-electro-chemical coupling mechanism can reflect the battery degradation from the material. In addition, the optimization of electrode design and improvement of battery performance are linked to economy. Therefore, this work can not only accurately estimate long-term SOH, but also provide parameters related to other battery performance analysis. Thirdly, compared with selecting voltage, current and charge discharge time as HIs, using the maximum solid-phase lithium-ion concentration of positive and negative electrodes as the model input can enhance the universality of neural network. Because the model using the above electrochemical parameters as input does not need to retrain the network with the change of working conditions. Fourthly, this work adopts self-designed energy storage working condition. Its inspiration comes from the peak-cutting and valley-filling conditions of actual energy storage power stations. At present, in other relevant references, the working conditions of energy storage LIBs are mostly vehicle working conditions. And this is not in line with the actual energy storage environment. Fifthly, in order to improve the search efficiency of the identification algorithm and avoid the algorithm falling into the local optimum as far as possible, this paper introduces a nonlinear decreasing adaptive chemotaxis behavior step size based on the BFO algorithm. Lastly, to improve the training accuracy of the back propagation neural network (BPNN), SA algorithm is introduced to optimize the

BPNN. Based on the BPNN, the SA-BP model introduces inferior initial parameters of BPNN through SA algorithm, so that the initial parameters of the network can avoid local optimization as far as possible.

Current demand and future development encourage to carry out this investigation. These two aspects can also well explain the impact and significance of the work on related research fields. The current demand is the clear motivation mentioned above. At current stage, manually updating the cell according to SOH can help energy storage stations maintain the normal operation. The future development is to optimize and improve LIBs in terms of materials. In the future, using more superior LIBs can improve the overall performance of the energy storage power station. By studying a series of electrochemical parameters, LIBs with superior performance can be manufactured.

The remainder of this paper is organized as follows. Section 2 presents the mathematical analysis, which includes the establishment of SP model, NDS-BFO parameter identification method, Pearson correlation analysis (PCA) method, grey correlation analysis (GRA) method and SA-BP modeling. Wherein, PCA and GRA methods are used to analyze the correlation and relational degree. The information of the experimental platform and results is described in Section 3. Finally, Section 4 summarizes the important conclusions and proposes the directions for future work.

## 2. Mathematical analysis

### 2.1. *The establishment of SP model*

LIB is a time-varying nonlinear energy storage system. Its internal electrochemical reaction mechanism is difficult to describe accurately. Therefore, in order to balance the computational complexity and model accuracy, it is important to establish a suitable battery model. Because the experiments are carried out under low-rate conditions, the establishment of the SP model can describe the dynamic characteristics of LIBs accurately. The SP model is a simplified electrochemical model that utilizes a single particle to characterize the battery. The diagram of the SP model is shown in Figure 1.

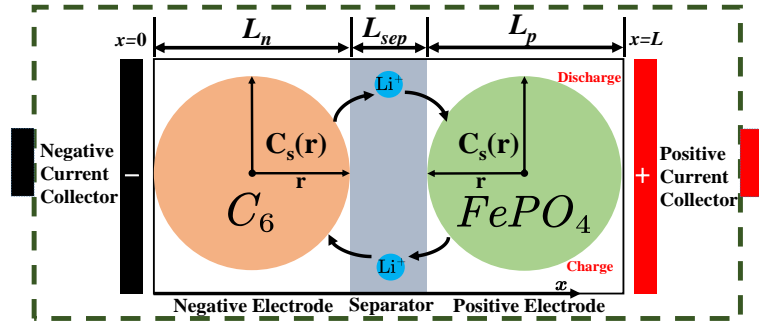


**Figure 1** Schematic diagram of SP model for LIBs

In Figure 1,  $x$  represents the thickness direction of the electrode and  $r$  represents the radius direction of the active particles in the electrode.  $L_n$ ,  $L_{sep}$  and  $L_p$  are the thicknesses of the negative electrode, the separator and the positive electrode, respectively. In the SP modeling, solid-phase diffusion, reaction polarization and ohmic polarization are the main processes. The molar reaction flux density expression at the boundary of the positive and negative current collectors is shown in Equation (1). In this paper,  $p$  represents the positive electrode, and  $n$  represents the negative electrode.

$$j_i = \frac{IR_{s,i}}{3F(1-\varepsilon_i - \varepsilon_{f,i})l_i A_i}, i = p, n \quad (1)$$

Among them,  $I$  is the battery current,  $R_{s,i}$  represents the radius of the particle,  $F$  represents the Faraday constant,  $\varepsilon_i$  represents the material porosity, and  $\varepsilon_{f,i}$  represents the filling substance volume fraction. Besides,  $l_i$  and  $A_i$  are the plate thickness and the effective area of pole piece, respectively.

From the physical mechanism of LIBs, it can be seen that the terminal voltage  $U_t$  can be calculated by the difference between the positive solid-phase potential  $\Phi_{s,p}$  and the negative electrode solid-phase potential  $\Phi_{s,n}$ . Combined with the main process of the SP modeling, the calculation formula of terminal voltage is shown in Equation (2).

$$U_t = \Phi_{s,p} - \Phi_{s,n} = E_p(\theta_p) + \eta_{act,p} + \eta_{ohm,p} - (E_n(\theta_n) + \eta_{act,n} + \eta_{ohm,n}) = E + \eta_{act} + \eta_{ohm} \quad (2)$$

Among them,  $E_i$  represents the positive or negative open-circuit potential,  $\theta_i$  is the utilization rate of positive or negative electrode,  $E$  is the battery open-circuit potential.  $\eta_{act,i}$  and  $\eta_{ohm,i}$  are the reaction polarization potential and

ohmic polarization potential of positive or negative electrode, respectively. In addition,  $\eta_{act}$  and  $\eta_{ohm}$  are the reaction polarization overpotential and ohmic polarization overpotential, respectively. Wherein, the expression of  $E$  is shown in Equation (3).

$$\begin{cases} E = E_p(\theta_p) - E_n(\theta_n) \\ \theta_p = \frac{c_{s,surf,p}}{c_{s,max,p}}, \theta_n = \frac{c_{s,surf,n}}{c_{s,max,n}} \end{cases} \quad (3)$$

Among them,  $c_{s,surf,i}$  and  $c_{s,max,i}$  represent the surface solid-phase lithium-ion concentration and the maximum solid-phase lithium-ion concentration, respectively. From Equation (3), it can be known that  $E$  is an expression about  $\theta_p$  and  $\theta_n$ . The solid-phase diffusion process of lithium ions can be described by applying Fick's second law in a spherical coordinate system. By using the three-parameter parabolic equation of solid-phase diffusion,  $c_{s,surf,i}$  can be obtained. After introducing the average solid-phase lithium-ion concentration  $c_{s,avg,i}$ ,  $c_{s,surf,i}$  and the average particle concentration flux  $q_{s,avg,i}$ , the solid-phase diffusion equation can be simplified by the three-parameter parabolic method, as shown in Equation (4).

$$\begin{cases} c_{s,avg,i}(t) = c_{s,0,i} - \int_0^t 3 \frac{j_i}{R_{s,i}} dt \\ \frac{d}{dt} q_{s,avg,i}(t) + 30 \frac{D_{s,i}}{R_{s,i}^2} q_{s,avg,i}(t) + \frac{45j_i}{2R_{s,i}^2} = 0 \\ c_{s,surf,i}(t) = c_{s,avg,i}(t) + (8D_{s,i}q_{s,avg,i}(t) - j_i) \frac{R_{s,i}}{35D_{s,i}} \\ c_{s,surf,i}(t)|_{t=0} = c_{s,surf,0,i}, \quad q_{s,avg,i}(t)|_{t=0} = 0 \end{cases}, i = n, p \quad (4)$$

Among them,  $c_{s,0,i}$  and  $c_{s,surf,0,i}$  represent the initial average solid-phase lithium-ion concentration and initial surface solid-phase Li-ion concentration.  $D_{s,i}$  and  $r$  represent the solid-phase lithium-ion diffusion coefficient and the radial distance coordinate of the particle. In Equation (2),  $\eta_{act}$  can be calculated by Equation (5).

$$\eta_{act} = \eta_{act,p} - \eta_{act,n} \quad (5)$$

Among them,  $\eta_{act,p}$  and  $\eta_{act,n}$  represent the reaction polarization overpotential of positive electrode and negative

electrode, respectively. The electrochemical reaction process of lithium ions at the solid-liquid interface in the positive and negative electrodes of LIBs can be described by Butler-Volmer kinetic equation, as shown in Equation (6).

$$\begin{cases} j_i = j_0 \left( \exp\left(\frac{\alpha F}{RT}\right) \eta_{act,i} - \exp\left(-\frac{\alpha F}{RT}\right) \eta_{act,i} \right) \\ j_0 = k_i \left( c_{s,max,i} - c_{s,surf,i}(t) \right)^{0.5} \left( c_{s,surf,i}(t) \right)^{0.5} c_e^{0.5} \end{cases}, i = p, n \quad (6)$$

Among them, the value of  $\alpha$  is 0.5. Besides,  $k_i$ ,  $c_e$ ,  $R$  and  $T$  represent the average electrode reaction rate constant, the liquid lithium-ion concentration, the universal gas constant and the battery temperature, respectively. By changing the form of Equation (6), the expression of  $\eta_{act,i}$  can be obtained, as shown in Equation (7).

$$\begin{cases} \eta_{act,i} = \frac{2RT}{F} \ln\left(m_i + \sqrt{m_i^2 + 1}\right) \\ m_i = \frac{j_i}{2k_i \left( c_{s,max,i} - c_{s,surf,i}(t) \right)^{0.5} \left( c_{s,surf,i}(t) \right)^{0.5} c_e^{0.5}} \end{cases} \quad (7)$$

According to the definition of SP model, the ohmic polarization process is mainly related to the solid electrolyte interphase (SEI) film. Therefore, the expression of  $\eta_{ohm}$  is shown in Equation (8).

$$\eta_{ohm} = \eta_{ohm,p} - \eta_{ohm,n} = R_{SEI,p} F j_p - R_{SEI,n} F j_n \quad (8)$$

Among them,  $R_{SEI,p}$  and  $R_{SEI,n}$  represent the SEI resistance of positive electrode and negative electrode, respectively. By combining Equation (2), (3), (7) and (8), the terminal voltage expression of SP model is shown in Equation (9).

$$U_t = E_p(\theta_p) - E_n(\theta_n) + \frac{2RT}{F} \frac{\ln\left(m_p + \sqrt{m_p^2 + 1}\right)}{\ln\left(m_n + \sqrt{m_n^2 + 1}\right)} + R_{SEI,p} F j_p - R_{SEI,n} F j_n \quad (9)$$

During the charge-discharge process, the SP model can be established, and the internal parameters can be solved according to this model. The block diagram of the SP model is shown in Figure 2.

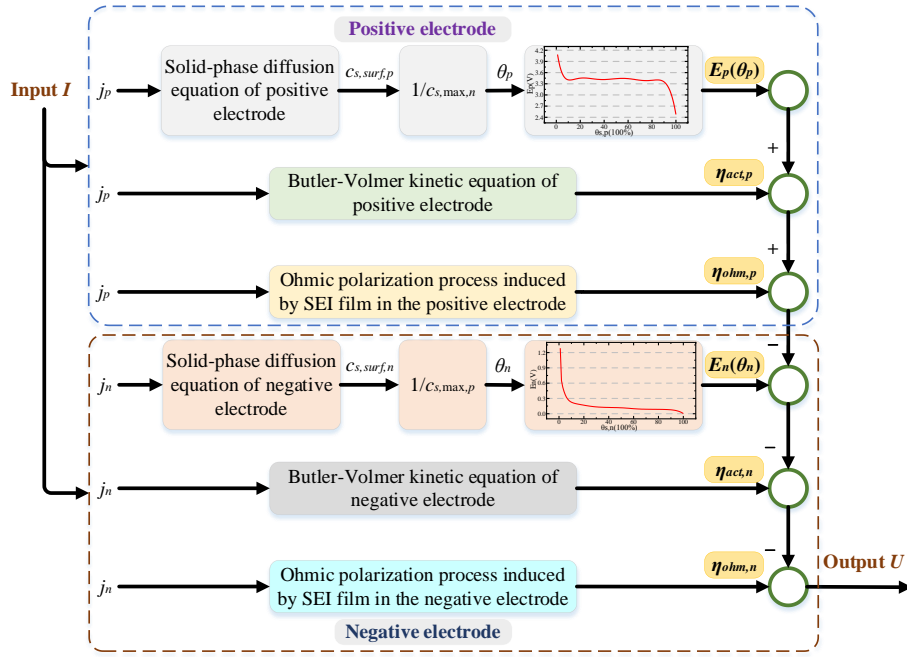


**Figure 2** The block diagram of the SP model

As can be seen from Figure 2, the block diagram of the SP model is described by the reaction of positive and negative electrodes. Among them,  $I$  and  $U$  represent the input current and output voltage. In addition, the two curve graphs included in Figure 2 represent the change of the positive/negative open-circuit voltage with the utilization rate of the positive/negative electrode.

## 2.2. NDS-BFO parameter identification method

In this paper,  $c_{s,max,p}$  and  $c_{s,max,n}$  are the two most importance electrochemical parameters, and their changes are directly related to the SOH of LIBs. And the NDS-BFO algorithm is selected to identify them. The main idea of identification is to minimize the variance between the measured terminal voltage and the simulated terminal voltage. Therefore, the objective function of identification is shown in Equation (10).

$$\min J(\theta) = \sum_{k=1}^n [V_k - f(I_k, \theta)]^2, \theta = (c_{s,max,p}, c_{s,max,n}) \quad (10)$$

Among them,  $k$  represents the sampling time,  $V_k$  represents the terminal voltage,  $I_k$  represents the current through the LIB,  $f(I_k, \theta)$  represents the fitting terminal voltage,  $\theta$  represents the set of parameters to be identified, and  $n$  represents the time at the end of sampling.

The core idea of BFO algorithm is that bacteria move away from or tend to the chemical substance by obtaining changes in the concentration of the chemical substance around it, so as to find the optimal solution. In a search space, the quality of bacteria can be determined by the fitness value. In this paper, Equation (10) is used as the fitness function of the BFO algorithm. The bacteria with small fitness values are healthy, and the corresponding identification results are accurate. The BFO algorithm simulates four intelligent behaviors of chemotaxis, swarming, reproduction, and elimination and dispersal.

The chemotaxis includes two behavior modes of tumble and swim. Tumble means bacteria moving in a new direction, and swim means bacteria keep moving in the same direction. The mode bacteria select to move depends on changes in surrounding nutrient concentrations. If the maximum number of movements is reached, the chemotaxis of the bacteria is stopped. After each chemotaxis, the updated value of  $\theta$  is shown in Equation (11).

$$\begin{cases} \theta^i(j+1, k, l) = \theta^i(j, k, l) + C(i)\varphi(i) \\ \varphi(i) = \frac{\Delta(i)}{\sqrt{\Delta^T(i)\Delta(i)}} \end{cases} \quad (11)$$

Among them,  $i$  represents the number of bacteria,  $j$  represents the number of chemotaxis behavior,  $k$  represents the number of reproduction behavior,  $l$  represents the number of elimination and dispersal behavior,  $C$  represents the step size of chemotaxis behavior,  $\varphi$  represents the direction vector of unit length, and  $\Delta$  represents a unit vector in random direction. In the process of bacterial foraging, individuals use attractants and repellants to achieve swarming behavior. The expression of swarming behavior among bacteria is shown in Equation (12).

$$\begin{aligned} J_{cc}(\theta) &= \sum_{i=1}^S J_{cc}^i(\theta) = \sum_{i=1}^S \left[ -d_a \exp\left(-\omega_a \sum_{m=1}^D (\theta_m - \theta_m^i)^2\right) \right] \\ &+ \sum_{i=1}^S \left[ h_r \exp\left(-\omega_r \sum_{m=1}^D (\theta_m - \theta_m^i)^2\right) \right] \end{aligned} \quad (12)$$

$J_{cc}$  is the influence value of signal transmission between bacteria,  $d_a$  is the amount of attractant,  $\omega_a$  is the diffusion rate of attractant,  $D$  is the search space dimension,  $\theta_m^i$  is the component of bacteria  $i$  in  $m$  space,  $\theta_m$  is the component of other bacteria in  $m$  space,  $h_r$  is the amount of repellant, and  $\omega_r$  is the diffusion rate of repellant.

Because the swarming behavior is introduced into the chemotaxis behavior, the corresponding fitness value of bacteria is updated, as shown in Equation (13).

$$J(i, j+1, k, l) = J(i, j, k, l) + J_{cc}(\theta^i(j+1, k, l)) \quad (13)$$

Among them,  $J$  is the fitness value. By Equation (13), bacteria can achieve the purpose of swarming after each chemotaxis behavior. After a period of foraging, some bacteria with weak ability to find food will be naturally eliminated. In order to maintain the same population size, the remaining bacteria will reproduce. This phenomenon is called reproduction in the algorithm. The health function is defined as the sum of fitness values during a periodic chemotaxis behavior, and its expression is shown in Equation (14).

$$J_h^i = \sum_{j=1}^{N_c+1} J(i, j, k, l) \quad (14)$$

Among them,  $N_c$  is the total step number of chemotaxis, and  $J_h$  is the health function of bacteria. The smaller the value of  $J_h$  is, the healthier the bacteria is. On this basis, half of the bacteria with poor health are eliminated, and the other half of the bacteria are reproduced. Changes in the environment may lead to the migration or elimination of bacterial populations. This phenomenon is called elimination and dispersal. In order to simulate this process, after several generations of reproduction, the bacteria are randomly dispersed with probability  $p_{ed}$ . The dispersed bacteria may be closer to the global optimal solution.

Aiming at the problem that the BFO algorithm may fall into local optimum, a nonlinear decreasing chemotaxis step size is proposed. The method can improve the search efficiency and avoid local optimization as much as possible. In this paper, a cosine function between 0 and  $\pi$  is used to describe the nonlinear change in the step size of the chemotaxis behavior. The improved step size expression is shown in Equation (15).

$$C(i, j) = \frac{C_{\max} - C_{\min}}{2} \cos \frac{\pi}{N_c} j + \frac{C_{\max} + C_{\min}}{2} \quad (15)$$

Among them,  $C_{\max}$  and  $C_{\min}$  are the maximum and minimum step size of chemotaxis behavior, respectively. It can be seen from Equation (15) that the function decreases slowly at the beginning, which is beneficial for

exploring the optimal solution with a larger step size at the initial stage of the algorithm. In addition, the decreasing rate of the function is also slow at the end, which is beneficial for a stable local search at the last stage of the algorithm to find the optimal solution. The steps of NDS-BFO algorithm are shown in Table 1.

**Table 1** Overview of NDS-BFO algorithm steps

Step1	The parameters in the NDS-BFO algorithm and the parameters to be identified are initialized.
Step2	The nonlinear decreasing step size is introduced into chemotaxis behavior.
Step3	The objective function is reduced by optimizing the parameters of chemotaxis behavior.
Step4	The parameters are screened by bacterial reproduction behavior.
Step5	The parameters are randomly dispersed with a certain probability through the elimination and dispersal behavior.
Step6	The value of the objective function corresponding to each parameter is calculated, and the minimum parameter of the objective function is the identification result.

In Table 1, *Step2* is the key step for improvement. Through the above steps, the optimal value of the parameter to be identified can be found as accurately as possible.

### 2.3. PCA and GRA methods

The selection of appropriate HIs is the primary issue when using NN models for SOH estimation of LIBs. In this paper, PCA and GRA methods are used to analyze the correlation and relational degree between the HIs and the SOH. Because the capacity definition method of SOH is adopted, the reference sequence can be replaced by capacity instead of SOH. PCA method is widely used to detect the linear correlation between two continuous variables. The core idea is to calculate the Pearson correlation coefficient. The Pearson correlation coefficient is defined as the quotient of covariance and standard deviation between two variables, as shown in Equation (16).

$$\rho_{X,Y} = \frac{\text{cov}(X,Y)}{\sigma_X \sigma_Y} = \frac{E((X - \mu_X)(Y - \mu_Y))}{\sigma_X \sigma_Y} = \frac{E(XY) - E(X)E(Y)}{\sqrt{E(X^2) - E^2(X)}\sqrt{E(Y^2) - E^2(Y)}} \quad (16)$$

Among them,  $X$  and  $Y$  represent two comparative sequences,  $\rho$  represents Pearson correlation coefficient,  $\text{cov}$  represents covariance,  $\sigma$  represents standard deviation and  $E$  represents mathematical expectation. Pearson correlation analysis has the advantage of fast calculation speed, but Pearson correlation coefficient can only measure the linear correlation between variables and lack the expression of other relationships. Therefore, the GRA method is introduced, and its basic idea is to reflect the relational degree between sequences by comparing

the similarity of curve shapes, which is a supplement to the shortcomings of Pearson correlation coefficient. The steps for the GRA method are shown in Table 2.

**Table 2** Overview of GRA method steps

	The reference and comparison sequences are determined, as shown in Equation (17).	
Step1	$\begin{cases} X_i = \{x_i(k)   k = 1, 2, \dots, n\} \\ Y = \{y(k)   k = 1, 2, \dots, n\} \end{cases}$	(17)
	Dimensionless processing is performed, which is shown in Equation (18).	
Step2	$x_{trans} = \frac{x}{\text{mean}(X)}$	(18)
	The relational coefficient between the reference sequence and the comparison sequence is calculated, as shown in Equation (19).	
Step3	$\begin{cases} \zeta_i(k) = \frac{\min_i \min_k \Delta_i(k) + \rho \min_i \min_k \Delta_i(k)}{\Delta_i(k) + \rho \min_i \min_k \Delta_i(k)} \\ \Delta_i(k) =  y(k) - x_i(k)  \end{cases}$	(19)
	The relational degree between the reference sequence and the comparison sequence is calculated, as shown in Equation (20).	
Step4	$r_i = \frac{1}{n} \sum_{k=1}^n \zeta_i(k), (k = 1, 2, \dots, n)$	(20)

Among them,  $X$  and  $Y$  represent the comparison sequence and the reference sequence, respectively,  $i$  is the number of the comparison sequence,  $k$  is the number of each point,  $n$  represents the sequence length,  $x$  is a certain value in the sequence,  $x_{trans}$  is the dimensionless value of  $x$ ,  $\zeta$  is the relational coefficient,  $\rho$  is the resolution coefficient, and  $r$  is the relational degree.

#### 2.4. SA-BP modeling

From the perspective of bionics, the NN model simulates the structure and characteristics of animal brain, and has a good effect on the description of nonlinear systems such as LIBs. Back propagation neural network is a multi-layer feedforward NN with error back propagation, which is often used in online estimation because of its simplicity. During the process of reaching the optimal value of the objective function, the forward propagation of the signal and the backward propagation of the error run through the whole BP model. In this paper, a three-layer BP model composed of input layer, hidden layer and output layer is selected, and its structure diagram is shown in Figure 3.

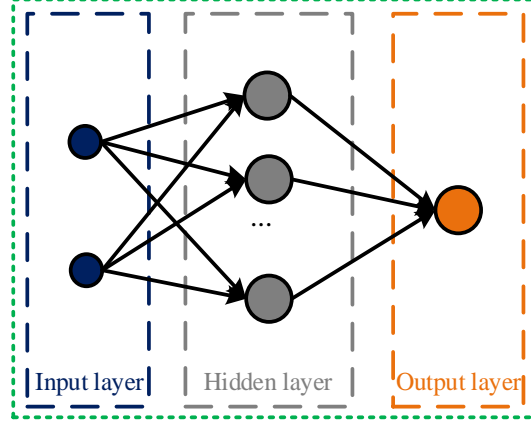


**Figure 3** The structure diagram of the three-layer BP model

Neurons are the basic structures in NN models. It can be seen from Figure 3 that the neurons in the adjacent layers are connected to each other, and the neurons in the same layer are independent of each other. The input and output relationship between adjacent layers is shown in Equation (21).

$$\begin{cases} net_j = \sum_{i=1}^n w_{ij}x_i - \theta \\ y_j = f(net_j) \end{cases} \quad (21)$$

Among them,  $net_j$  represents the value of weighted input to neuron  $j$ ,  $w_{ij}$  represents the weight from neuron  $i$  to neuron  $j$ ,  $x_i$  represents the signal transmitted from the last neuron,  $\theta$  is the threshold,  $f()$  is the activation function,  $y_j$  represents the output value of neuron  $j$ , and  $n$  represents the number of neurons received by neuron  $j$ . After completing the forward propagation of the data, the estimated output  $y_{BP,k}$  will have a large gap with the expected output  $y_{t,k}$ . Therefore, the square error function is selected as the loss function of the BP model, and the total error  $E$  can be obtained through the loss function, which is shown in Equation (22).

$$E = \frac{1}{2} \sum_{k=1}^N (y_{t,k} - y_{BP,k})^2 \quad (22)$$

Among them,  $k$  is the number of the sample, and  $N$  is the number of neurons in the output layer. The connection weights are adjusted by learning rules. Common learning rules include gradient descent method, Gauss-Newton

method, and Levenberg-Marquardt (L-M) method. The corresponding calculation formula of the weight change is also different by using different learning rules.

Because the BP model might obtain the local optimal solution of the weight, the SA algorithm is introduced to optimize the calculation process of the weight. The basic idea of SA algorithm originates from the annealing process of solid matter in physics. In the search process, the algorithm adds the escape probability to introduce inferior solutions, so that the results can avoid local optimization as far as possible. The steps of the SA algorithm can be summarized as shown in Table 3.

**Table 3** Overview of SA algorithm steps

Step1	The temperature $T$ , the solution $S$ , and the number of iterations $L$ are initialized.
Step2	A new solution $S_{new}$ is randomly selected near the current optimal solution $S$ , and the cost function $C(S)$ and $C(S_{new})$ are calculated. The expression of the $C$ is the same as Equation (22). The cost function increment $\Delta C$ is calculated, as shown in Equation (23).
Step3	$\Delta C = C(S_{new}) - C(S) \quad (23)$
Step4	According to the Metropolis criterion, $S_{new}$ is accepted as the optimal solution with probability $P$ , otherwise $S$ is maintained as the optimal solution. The expression of $P$ is shown in Equation (24). $P = \begin{cases} 1 & , \Delta C < 0 \\ e^{-\frac{\Delta C}{T}} & , \Delta C > 0 \end{cases} \quad (24)$
Step5	The iteration of $L$ is carried out at the current temperature, that is, the inner loop of <i>Step2</i> to <i>Step4</i> is performed. The temperature $T$ is decreased at a certain speed, as shown in Equation (25).
Step6	$T_{new} = \lambda T, 0 < \lambda < 1 \quad (25)$
Step7	After updating the temperature, the outer loop from <i>Step2</i> to <i>Step6</i> is performed until the termination condition is met, and the current solution is output as the optimal solution.

Among them,  $\lambda$  is the temperature drop rate, and  $T_{new}$  is the temperature value after one update. In this paper, the main function of SA algorithm is to optimize the initial parameters of BP model. The weights and thresholds after iterative update are adopted as a new starting point for BP training. Therefore, the whole process of the SA-BP model can be described in Table 4.

**Table 4** Overview of SA-BP model

Step1	The structure and parameters of the SA-BP model are initialized.
Step2	The BP parameters are optimized by Table 3.
Step3	The optimal weights and thresholds are input into the BP model.

Combined with the establishment of SP model, NDS-BFO parameter identification method, PCA method, GRA method and SA-BP modeling, the flowchart of the long-term SOH estimation for LIBs proposed in this paper is shown in Figure 4.

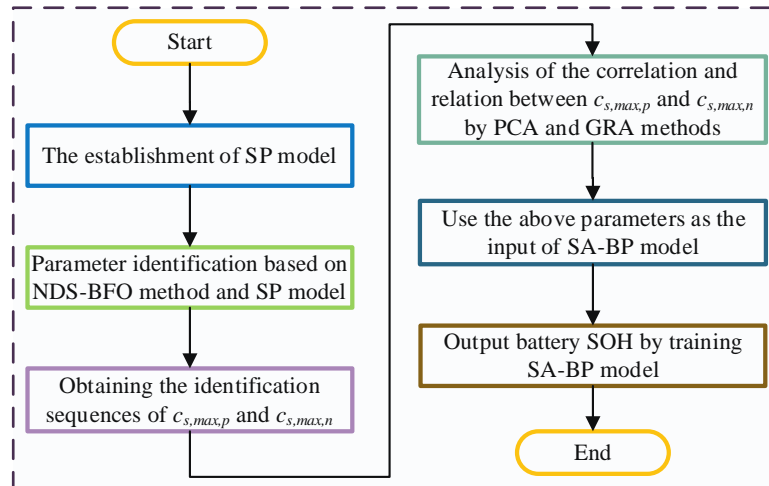


**Figure 4** The flowchart of the long-term SOH estimation for LIBs

As can be seen from Figure 4, the proposed algorithm combines the EM and the data-driven method, and uses the HIs with high correlation of capacity as the BP input to obtain the SOH during the degradation process.

### 3. Experimental analysis

#### 3.1. Test platform and experimental setup

In this paper, four 26650 lithium iron phosphate batteries with rated capacity of 2.3Ah were used for experiments. And all the operation steps are strictly carried out under a power battery high-rate charge-discharge tester (BTS750-200100-4) and a temperature-controlled thermostat (BTKS5-150C). In addition, the experimental data is transmitted to the host computer through charge-discharge tester for storage. The structure of the experimental platform is shown in Figure 5.

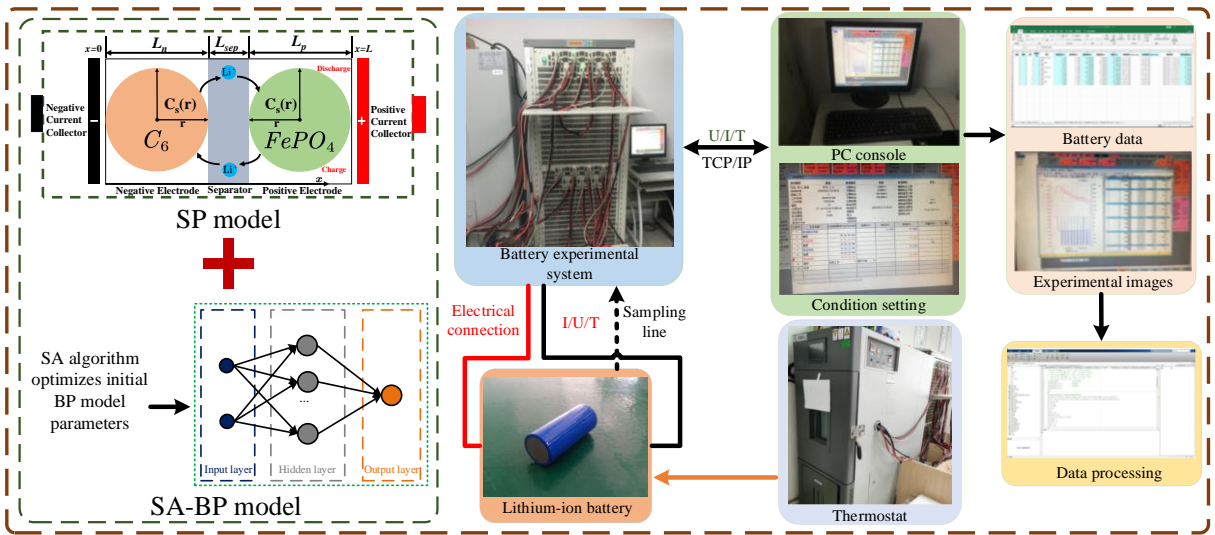


**Figure 5** The structure of the experimental platform

The temperature of the thermostat is set to 25 °C under all experimental conditions. The personal computer (PC) for performing all algorithms is configured as follows: Intel (R) Core (TM) i5-9500 CPU 3.00 GHz and NVIDIA GeForce GT 710 GPU with 24 GB memory. The experiments to be performed include the 0.1 C constant current test of one cell, the 0.5 C constant current degradation experiment of two cells, and the energy storage degradation experiment of one cell. Under the 0.5 C constant current degradation experiment, the cell used for model training is marked *Cell1*, and another cell is marked *Cell2*. The cell under the energy storage degradation experiment is marked *Cell3*. In addition, the cell under the 0.1 C constant current degradation experiment is marked *Cell4*. Among them, the 0.1 C constant current condition is used to verify the SP model and obtain the positive open-circuit potential expression. Besides, the energy storage degradation condition is obtained by the actual peak-cutting and valley-filling conditions. In the above expression, C represents the battery charge-discharge rate. The current curve within one cycle in the energy storage degradation experiment is shown in Figure 6.

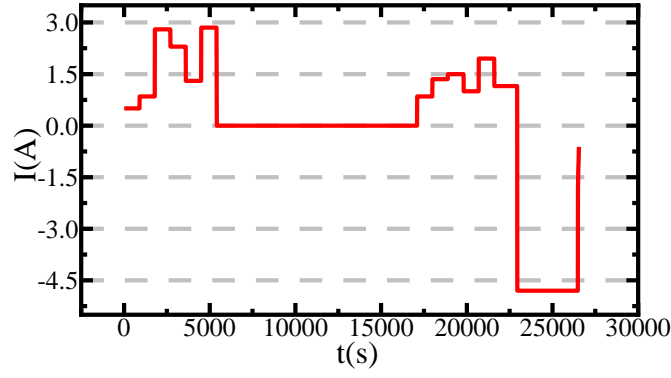


**Figure 6** The current curve within one cycle in the energy storage degradation experiment

In Figure 6, the current during charge process is negative, and the current during discharge process is positive.

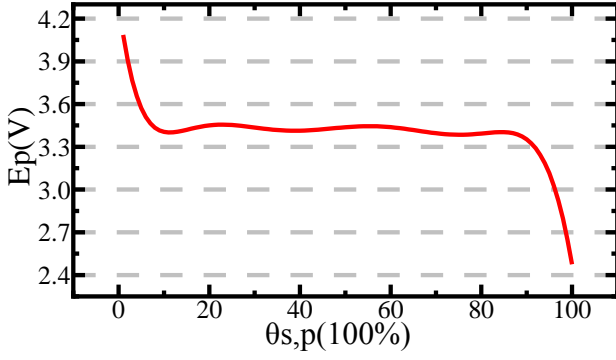
And it is necessary to obtain the maximum discharge capacity every ten cycles.

### 3.2. Identification results and model verification

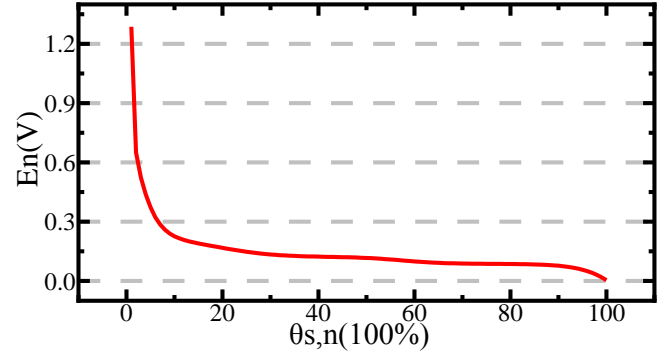
As can be known from Section 2.1, it is essential to get the expressions of positive and negative open-circuit potential for the SP model establishment. The negative open-circuit potential can be expressed by empirical formula. Under the 0.1 C constant current test, the expression of positive open-circuit potential can be fitted by combining the empirical formula and the difference of voltages. In this paper, the expressions of negative and positive open-circuit potential are shown in Equation (26).

$$\begin{cases}
 E_n(\theta_{s,n}) = 0.6379 + 0.5416e^{-305.5309\theta_{s,n}} + 0.044 \tanh\left(\frac{-(\theta_{s,n} - 0.1958)}{0.1088}\right) - 0.1978 \tanh\left(\frac{\theta_{s,n} - 1.0571}{0.0854}\right) \\
 -0.6875 \tanh\left(\frac{\theta_{s,n} + 0.0117}{0.0529}\right) - 0.0175 \tanh\left(\frac{\theta_{s,n} - 0.5692}{0.0875}\right) \\
 E_p(\theta_{s,p}) = 509.049\theta_{s,p}^8 - 2584.678\theta_{s,p}^7 + 5232.112\theta_{s,p}^6 - 5526.454\theta_{s,p}^5 + 3311.622\theta_{s,p}^4 \\
 -1138.272\theta_{s,p}^3 + 214.763\theta_{s,p}^2 - 19.752\theta_{s,p} + 4.0857
 \end{cases} \quad (26)$$

According to Equation (26), the curves of positive and negative open-circuit potential with the changes of utilization of electrodes can be obtained, as shown in Figure 7.



(A) The open-circuit potential curve of the positive electrode



(B) The open-circuit potential curve of the negative electrode

**Figure 7** The open-circuit potential curves of the positive and negative electrodes

It can be seen from Equation (9) that some electrochemical parameters need to be obtained for SP modeling.

The specific values of the relevant parameters are shown in Table 5.

**Table 5** Some electrochemical parameters in the SP model

Parameter type	Symbol	Value (25°C)	Symbol	Value (25°C)
Faraday constant (C/mol)	$F$	96487	$F$	96487
Universal gas constant (J/mol/K)	$R$	8.314	$R$	8.314
Battery temperature (K)	$T$	298.15	$T$	298.15
Plate thickness (m)	$l_p$	$70 \times 10^{-6}$	$l_n$	$34 \times 10^{-6}$
Effective area of pole piece (m <sup>2</sup> )	$A_p$	0.17	$A_n$	0.17
The radius of the active particle (m)	$R_{s,p}$	$3.65 \times 10^{-8}$	$R_{s,n}$	$3.5 \times 10^{-6}$
Solid-phase diffusion coefficient (m <sup>2</sup> /s)	$D_{s,p}$	$1.18 \times 10^{-18}$	$D_{s,n}$	$2 \times 10^{-14}$
Ohmic resistance induced by SEI film ( $\Omega \cdot m^2$ )	$R_{SEI,p}$	0.001	$R_{SEI,n}$	0.001
Material porosity	$\varepsilon_p$	0.3	$\varepsilon_n$	0.47
Filling substance volume fraction	$\varepsilon_{f,p}$	0.26	$\varepsilon_n$	0.03
Average electrode reaction rate constant (m <sup>2.5</sup> mol <sup>-0.5</sup> s <sup>-1</sup> )	$k_p$	$3 \times 10^{-11}$	$k_n$	$8.19 \times 10^{-12}$
Liquid-phase Li-ion concentration (mol/m <sup>3</sup> )	$c_{e,p}$	1000	$c_{e,n}$	1000
Initial surface solid-phase Li-ion concentration (mol/m <sup>3</sup> )	$c_{s,surf,0,p}$	3900	$c_{s,surf,0,n}$	14870

Combining Equation (26), Table 5 and Equation (9), a terminal voltage expression only for  $c_{s,max,p}$  and  $c_{s,max,n}$  can

be obtained. When using the NDS-BFO algorithm for parameter identification, the relevant parameters are set as

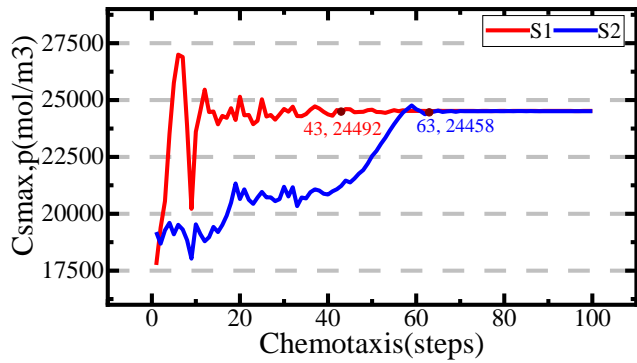
shown in Table 6.

**Table 6** The relevant parameters of NDS-BFO algorithm

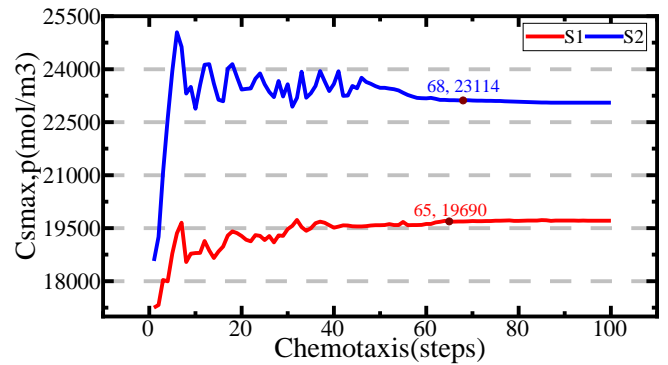
Parameter	Symbol	Value
The maximum positive solid-phase Li-ion concentration (mol/m <sup>3</sup> )	$c_{s,max,p}$	[16000,27000]
The maximum negative solid-phase Li-ion concentration(mol/m <sup>3</sup> )	$c_{s,max,n}$	[23000,36000]
Total number of bacteria	$S$	20
Total steps of chemotaxis	$N_c$	100
The maximum value of step size for chemotaxis	$C_{max}$	100

The minimum value of step size for chemotaxis	$C_{min}$	2
The maximum step for each progress in chemotaxis	$N_s$	5
Number of reproduction	$N_{re}$	8
Number of elimination and dispersal	$N_{ed}$	2
probability of elimination and dispersal	$P_{ed}$	0.25
The amount of attractant	$d_a$	0.05
The diffusion rate of attractant	$\omega_a$	0.05
The amount of repellant	$h_r$	0.05
The diffusion rate of repellant	$\omega_r$	2

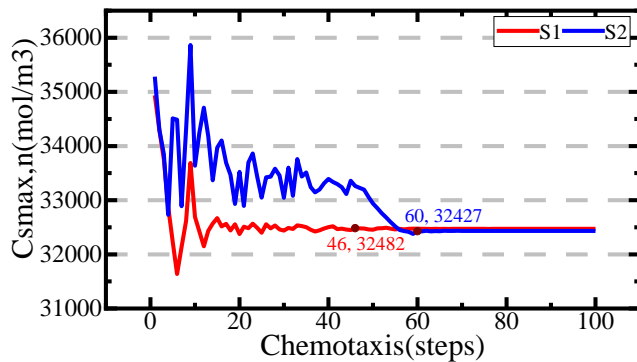
The identification results of  $c_{s,max,p}$  and  $c_{s,max,n}$  in each degradation cycle can be obtained by combining Equation (26), Table 5, Equation (9) and Table 6. Because the electrochemical parameters of *Cell1* are used to train the SOH estimation model, the relevant identification process should be described in detail. To verify the improvement effect of NDS-BFO algorithm, the identification results and fitness values of NDS-BFO algorithm and BFO algorithm are analyzed. In the first degradation and last degradation of *Cell1*, the analysis results using NDS-BFO algorithm and BFO algorithm are shown in Figure 8.



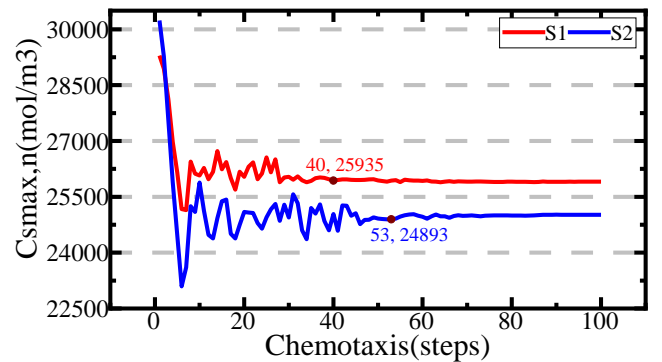
(A) Identification process of  $c_{s,max,p}$  during the first degradation cycle



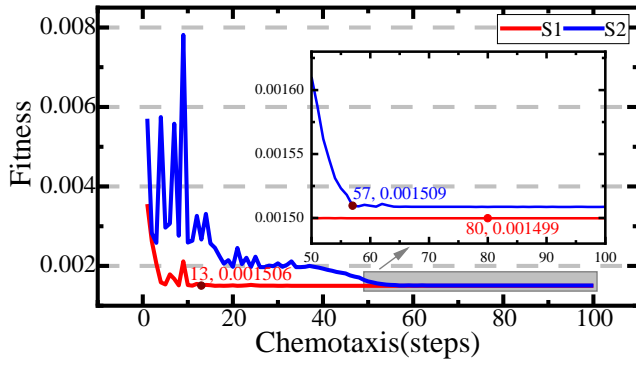
(B) Identification process of  $c_{s,max,p}$  during the last degradation cycle



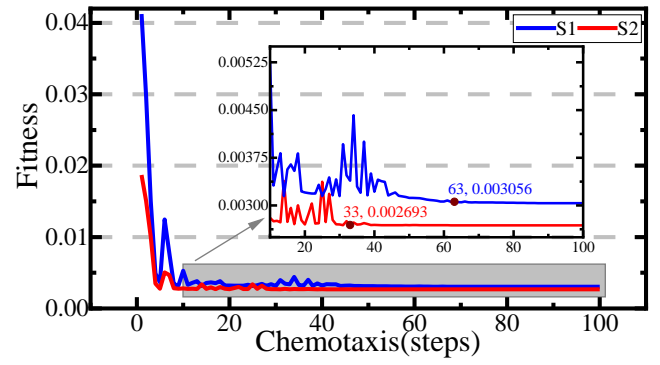
(C) Identification process of  $c_{s,max,n}$  during the first degradation cycle



(D) Identification process of  $c_{s,max,n}$  during the last degradation cycle



(E) The fitness during the first degradation cycle



(F) The fitness during the last degradation cycle

**Figure 8** Identification results of NDS-BFO algorithm and BFO algorithm

In Figure 8, S1 and S2 represent NDS-BFO algorithm and BFO algorithm, respectively. In the first cycle, it can be seen from Figure 8A,C that the improved algorithm converges faster when identifying  $c_{s,max,p}$  and  $c_{s,max,n}$ . Besides, it can be seen from Figure 8E that in the first cycle, the fitness of the improved algorithm can converge after 13 iterations, while the BFO algorithm needs 57 iterations to converge. On the PC used in this work, the calculation time for BFO algorithm to reach convergence fitness is 317.18 s, and the corresponding time for NDS-BFO algorithm is 77.36 s. In addition, the optimal fitness value of the improved identification algorithm is smaller. In the last cycle, it can be seen from Figure 8B,D that the identification results of the two algorithms differ greatly. This shows that the results of one of the algorithms fall into the local optimum. In addition, it can be seen from Figure 8F that the improved algorithm has faster convergence speed and smaller fitness value. This proves that the improved algorithm can solve the problem that the identification results of BFO algorithm are locally optimal. All the above discussions verify the advantages of NDS-BFO algorithm compared with BFO algorithm. It is worth noting that the fitness value obtained by the same identification algorithm increases after battery degradation. And this result reflects that the accuracy of  $c_{s,max,p}$  and  $c_{s,max,n}$  obtained by degraded SP voltage model has decreased. Because  $c_{s,max,p}$  and  $c_{s,max,n}$  are input parameters for estimating SOH, the degraded SP voltage model can affect the accuracy of SOH estimation results. In the process of battery degradation, the electrochemical parameter identification results of  $Cell1$  obtained by NDS-BFO algorithm are shown in Figure 9.

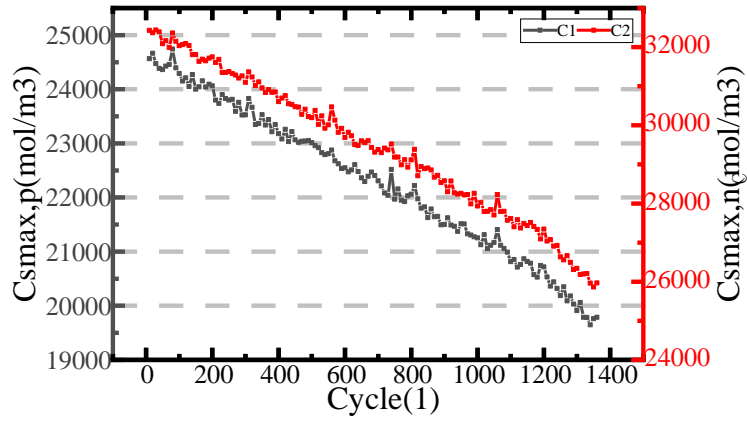
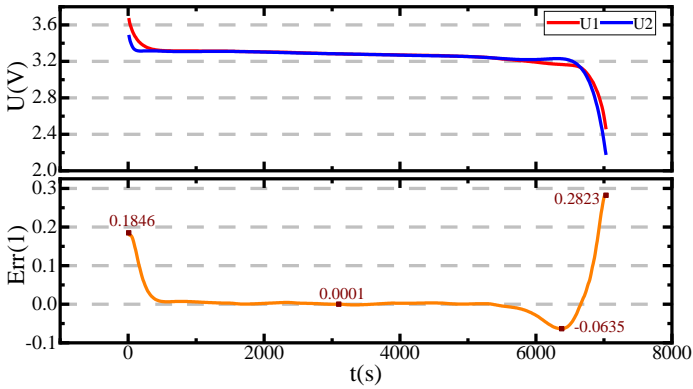
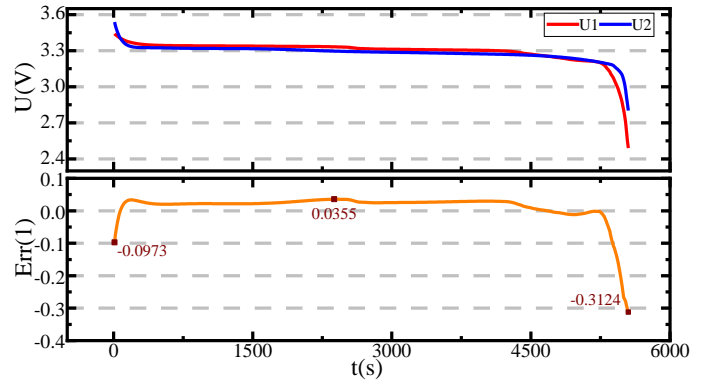


**Figure 9** The identification results of  $c_{s,max,p}$  and  $c_{s,max,n}$

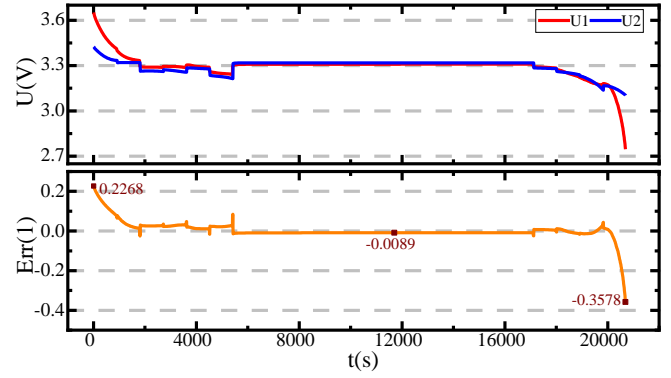
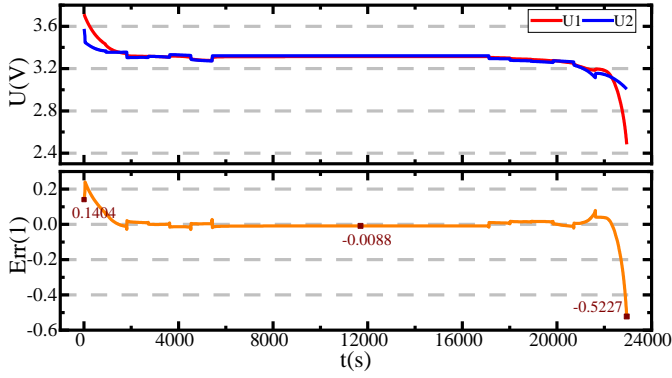
As can be seen from Figure 9, both  $c_{s,max,p}$  and  $c_{s,max,n}$  show a decreasing trend with the battery degradation. Because *Cell1* and *Cell2* are tested under the same working conditions, only the SP voltage models of *Cell2*, *Cell3* and *Cell4* are verified. Among them, *Cell2* and *Cell3* carry out long-term degradation experiments, so the actual and simulated terminal voltages of these two cells in the first cycle and the last cycle are selected for model verification. In addition, *Cell4* carries out one cycle charge-discharge experiment, so the model in this cycle is verified. The terminal voltages and the errors of *Cell2*, *Cell3* and *Cell4* are shown in Figure 10.



(A) The terminal voltages and the errors of *Cell2* during the first cycle

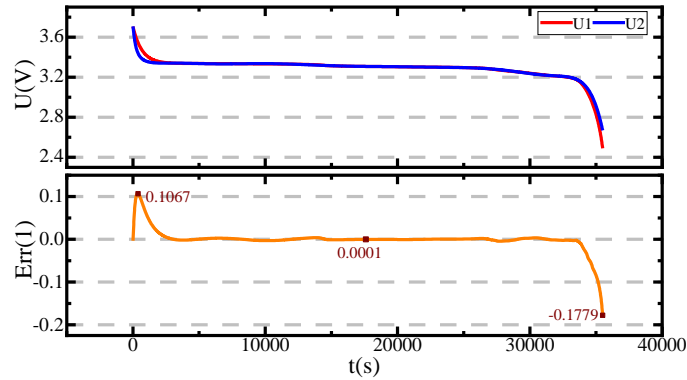


(B) The terminal voltages and the errors of *Cell2* during the last cycle



(C) The terminal voltages and the errors of *Cell3* during the first cycle

(D) The terminal voltages and the errors of *Cell3* during the last cycle



(E) The terminal voltages and the errors of *Cell4*

**Figure 10** The terminal voltages and the errors under two constant conditions

In Figure 10,  $U_1$  and  $U_2$  represent the measured terminal voltage and the simulated terminal voltage, respectively. Compared Figure 10A with B or compared Figure 10C with D, it can be seen that, after degradation, the discharge time during a single cycle is reduced. In addition, it can be seen from Figure 10 that the terminal voltage simulation effects of the three cells are good. The MAEs of terminal voltages are shown in Table 7.

**Table 7** The MAEs of terminal voltages

Cell	First cycle	Last cycle
<i>Cell2</i>	0.019V	0.0297V
<i>Cell3</i>	0.0208V	0.0256V
<i>Cell4</i>	0.0078V	/

It can be seen from Table 7 and Figure 10 that the accuracy of the SP voltage model decreases slightly during the degradation process. This result reflects that the identification errors of  $c_{s,max,p}$  and  $c_{s,max,n}$  increase. Because the above electrochemical parameters are used as the input of the SOH estimation model, their increase may deteriorate the accuracy of the SOH estimation model. In addition, the simulation results of *Cell4* are better than

that of *Cell2*, which confirms that the SP model has better simulation effect at lower rate.

### 3.3. Correlation coefficient and relational degree analysis

With  $c_{s,max,p}$  and  $c_{s,max,n}$  as the comparison sequences, and taking the capacity as the reference sequence, PCA and GRA methods are used to analyze the correlation coefficient and relational degree, respectively. Wherein, the resolution coefficient in the GRA method is 0.5. The correlation coefficient and relational degree between above electrochemical parameters and battery capacity are shown in Table 8.

**Table 8** The correlation coefficient and relational degree

Parameter	Correlation coefficient	Relational degree
$c_{s,max,p}$	0.9955	0.7013
$c_{s,max,n}$	0.9966	0.7206

It can be seen from Table 8 that the correlation coefficient and relational degree are relatively high. In addition, taking  $c_{s,max,p}$  and  $c_{s,max,n}$  as HIs can enhance the versatility of the NN model. The model which takes the voltage, current and charge-discharge time as the HIs can only satisfy the training under a specific working condition. When the working condition changes, the trained network is no longer applicable, and a new network training is required. This requirement is inappropriate in actual projects. However, the SOH estimation model based on  $c_{s,max,p}$  and  $c_{s,max,n}$  can provide accurate estimation for a variety of working conditions.

### 3.4. SOH analysis under complex conditions

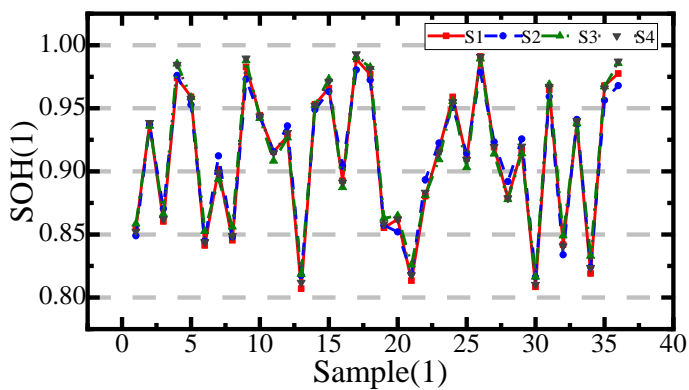
The *Cell1* capacity degrades to 80% of the initial state after 1360 cycles. Therefore, there are 136 groups of data with  $c_{s,max,p}$  and  $c_{s,max,n}$  as input and SOH as output. Among the 136 groups of data, 100 groups of random data are selected as the training set of the SA-BP model, and the remaining groups are used as the test set. The initial parameter settings in the SA-BP model are shown in Table 9.

**Table 9** The initial parameter settings in the SA-BP model

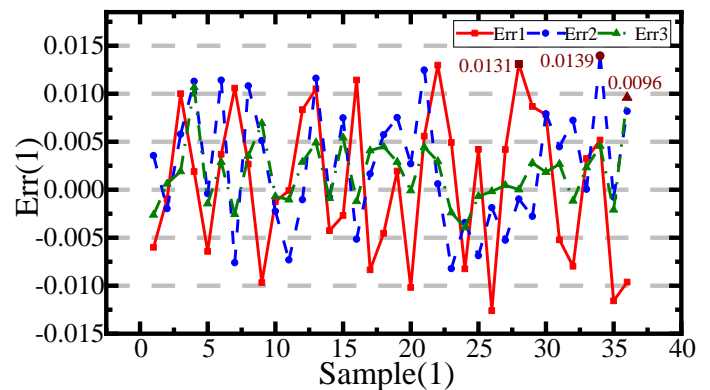
Parameter	Symbol	Value/Type
Initial temperature (°C)	$T_0$	10
Final temperature (°C)	$T_f$	1
Temperature decay scale	$\lambda$	0.85
Step factor	$c$	0.2
Markov length	$L$	10

Number of input layer nodes	/	2
Number of hidden layer nodes	/	5
Number of output layer nodes	/	1
Learning rule	/	L-M
Learning rate	/	0.01
The maximum number of iterations	/	100
target mean squared error	/	$1 \times 10^{-3}$
The activation function of the hidden layer	/	Sigmoid
The activation function of the output layer	/	Purelin

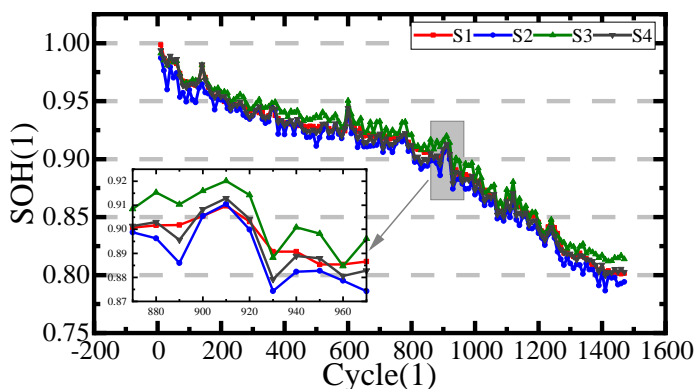
When the number of iterations exceeds the setting maximum value, or the target mean square error meets the requirements, the training is stopped. The weights and thresholds of the network are stored for the test set. In addition, all the data of *Cell1* are used as the training set, and all the data of *Cell2* and *Cell3* are used as the test set. Among them, *Cell2* is tested under 0.5 C constant current degradation condition, and *Cell3* is tested under the energy storage degradation condition. The output SOH and the corresponding errors of the three cells are shown in Figure 11.



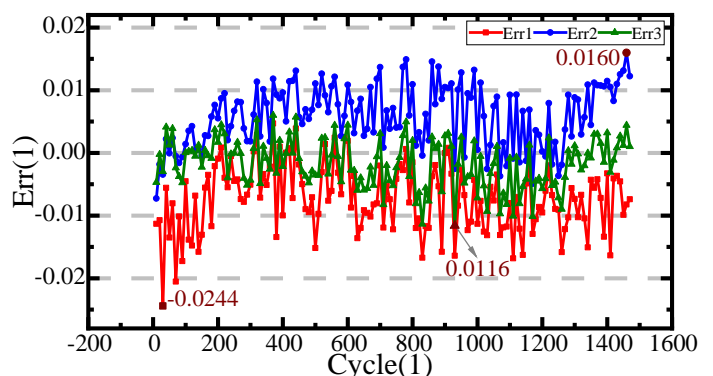
(A) Estimated and actual SOH values of *Cell1*



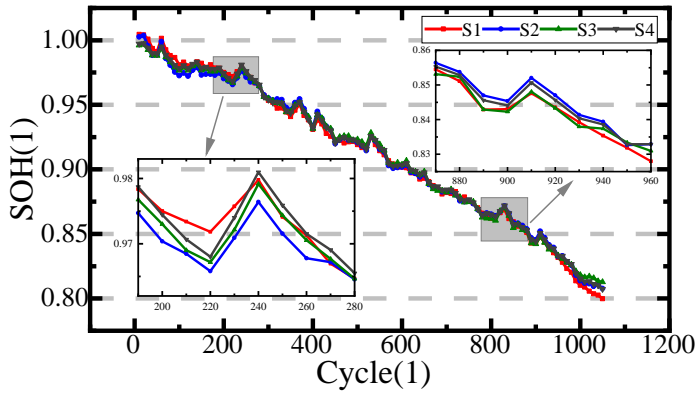
(B) The SOH errors of *Cell1*



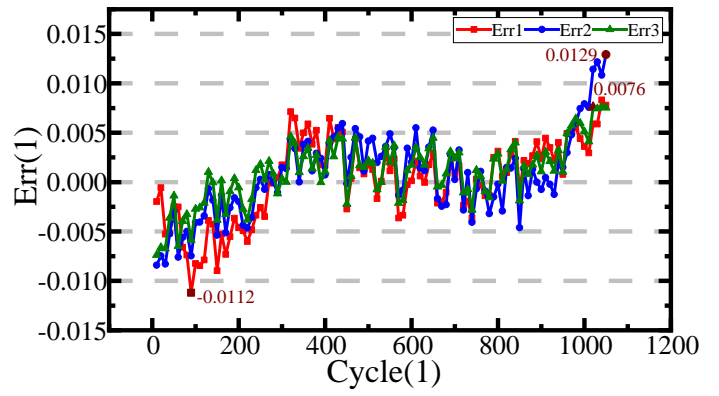
(C) Estimated and actual SOH values of *Cell2*



(D) The SOH errors of *Cell2*



(E) Estimated and actual SOH values of *Cell3*



(F) The SOH errors of *Cell3*

**Figure 11** SOH values and errors of test sets

In Figure 11A,C,E, S1, S2, S3 and S4 represent the actual SOH value, the estimated value of the nonlinear decreasing step-bacterial foraging optimization-back propagation (NDS-BFO-BP) algorithm, the estimated value of the nonlinear decreasing step-bacterial foraging optimization-Elman (NDS-BFO-Elman) algorithm and the estimated value of the nonlinear decreasing step-bacterial foraging optimization-simulated annealing-back propagation (NDS-BFO-SA-BP) algorithm, respectively. Among them, the parameters of Elman neural network are set as in Table 9. In Figure 11B,D,F, Err1, Err2 and Err3 represent the estimation errors of NDS-BFO-BP algorithm, NDS-BFO-Elman algorithm and NDS-BFO-SA-BP algorithm, respectively. The performance evaluation indicators of different algorithms are shown in Table 10.

**Table 10** The performance evaluation indicators of different algorithms

Algorithm type	<i>Cell1</i>	<i>Cell2</i>	<i>Cell3</i>
NDS-BFO-BP	RMSE:0.762%	RMSE:0.909%	RMSE:0.414%
	MAE:0.668%	MAE:0.772%	MAE:0.339%
	MAPE:0.738%	MAPE:0.872%	MAPE:0.371%
NDS-BFO-Elman	RMSE:0.667%	RMSE:0.768%	RMSE:0.429%
	MAE:0.545%	MAE:0.649%	MAE:0.333%
	MAPE:0.612%	MAPE:0.722%	MAPE:0.369%
NDS-BFO-SA-BP	RMSE:0.374%	RMSE:0.420%	RMSE:0.330%
	MAE:0.288%	MAE:0.336%	MAE:0.265%
	MAPE:0.314%	MAPE:0.377%	MAPE:0.294%

From Table 10, it can be seen that the method based on NDS-BFO algorithm and SA-BP model is obviously better than the other two algorithms in the error indicators of RMSE, MAE and MAPE. However, the above results

can only prove the accuracy of the SA-BP model. Therefore, in order to verify the superiority of NDS-BFO algorithm, bacterial foraging optimization-simulated annealing-back propagation (BFO-SA-BP) algorithm is used to compare with the proposed algorithm. The output SOH of *Cell2* and *Cell3* and their errors are shown in Figure 12.

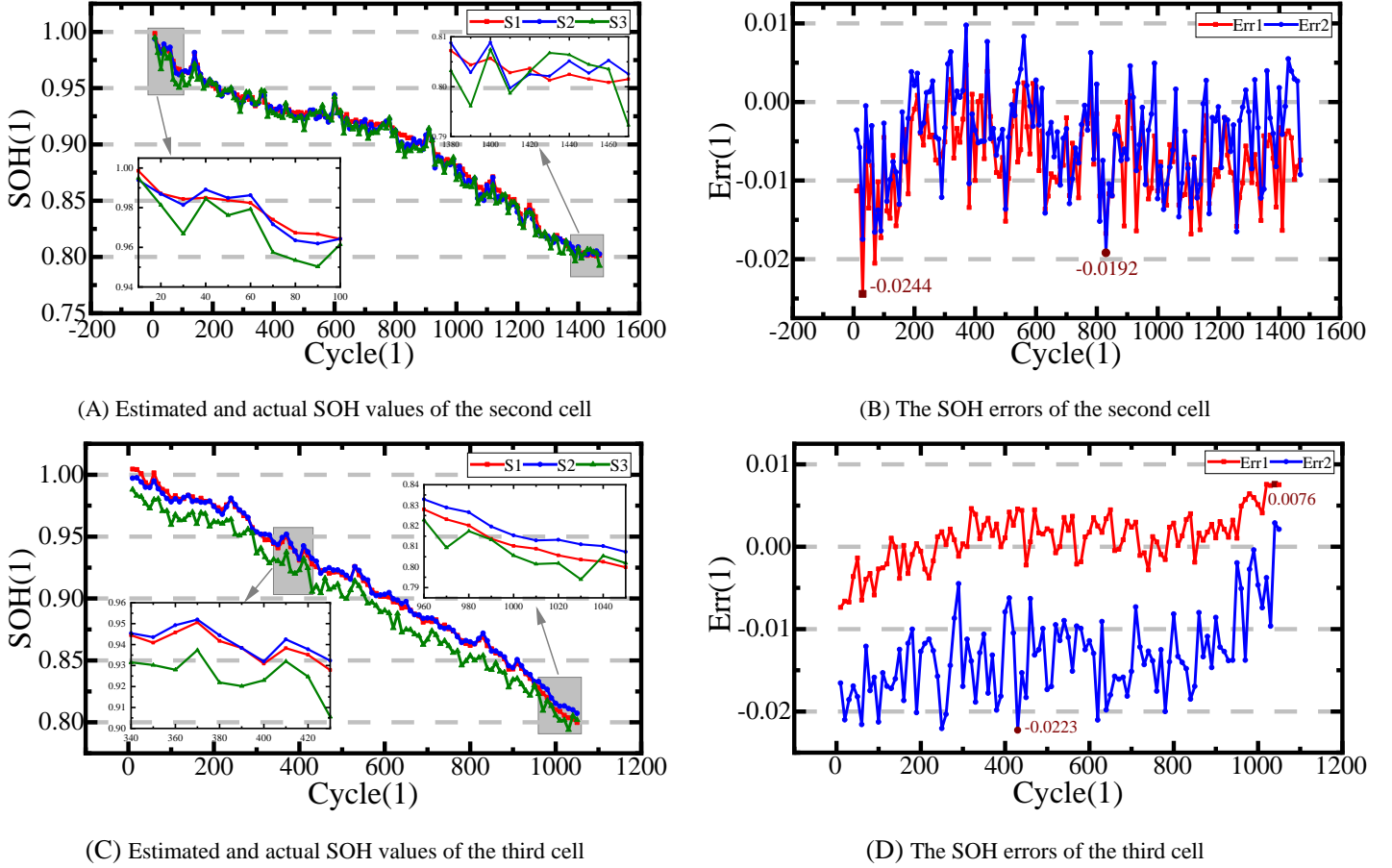


**Figure 12** SOH values and errors of test sets during degradation

In Figure 12A,C, S1, S2, and S3 represent the actual SOH value, the estimated value of NDS-BFO-SA-BP algorithm and the estimated value of BFO-SA-BP algorithm, respectively. And in Figure 12B,D, Err1 and Err2 represent the estimation errors of NDS-BFO-SA-BP algorithm and BFO-SA-BP algorithm, respectively. The performance evaluation indicators of the two algorithms are shown in Table 11.

**Table 11** The performance evaluation indicators of the above two algorithms

Algorithm type	<i>Cell2</i>	<i>Cell3</i>
BFO-SA-BP	RMSE:0.737%	RMSE:1.427%
	MAE:0.591%	MAE:1.330%
	MAPE:0.662%	MAPE:1.471%

NDS-BFO-SA-BP	RMSE:0.420%	RMSE:0.330%
	MAE:0.336%	MAE:0.265%
	MAPE:0.377%	MAPE:0.294%

It can be seen from Table 11 that the proposed algorithm is still superior in RMSE, MAE and MAPE. By analyzing Table 10 and Table 11, it can be known that the proposed algorithm has better nonlinear mapping ability. And this result proves that the proposed algorithm can more accurately simulate the long-term SOH. Besides, it can be seen from Figure 11 and Figure 12 that, with the deterioration of SP voltage model, the SOH and the estimation accuracy of SOH decrease. The above results highlight the superior improvement effects of the proposed algorithm in estimating the SOH of energy storage LIBs. Additionally, in order to verify the performance of the proposed algorithm, it is compared with the existing SOH estimation methods, as shown in Table 12. Among them, the existing methods include ENN, LSTM, DCNN, BPNN, cuckoo search-Elman neural network (CS-ENN) and gate recurrent unit-neural network (GRUNN).

**Table 12** The comparison of different SOH estimation methods

SOH estimation methods	Refs.	His	RMSE	MaxE	MAE	MAPE
End-to-end	ENN [89]	Constant current charging time, constant voltage charging time, voltage change during charging and discharge, total discharge time and temperature change during discharge	3.075%	-	2.0936%	1.6%
	LSTM [90]	Constant current time, constant voltage time, constant current time proportion, constant voltage time proportion and total charge time	0.762%	-	0.652%	-
	DCNN [48]	Voltage, current and capacity during partial charge cycles	0.368%	3.524%	-	-
BPNN [41]	Parameters of the first-order equivalent circuit model	-	7.2%	<5%	-	
CS-ENN [91]	Four principal components consisting of EIS features	0.74%	-	0.53%	0.69%	
Non-end-to-end	ENN [91]	Four principal components consisting of EIS features	1.74%	-	1.64%	2.12%
	GRUNN [92]	Six HIs from the differential temperature curves	-	2.28%	-	-
Proposed method	/	Maximum solid-phase lithium-ion concentration of positive and negative electrodes	0.33%	-	0.265%	0.294%

In Table 12, the comparison covers RMSE, maximum error (MaxE), MAE, MAPE and HIs. By comparing the

SOH estimation accuracy of the methods in Table 12, it can be seen that the proposed method is superior in multiple estimation performance indicators. Besides, by comparing the HIs and estimation results of the two ENN methods in the table, it can be seen that the results of non-end-to-end ENN are better than that of end-to-end ENN. To some extent, this demonstrates that the appropriate non-end-to-end model has a better effect in estimating SOH.

#### 4. Conclusions

In order to monitor the SOH of energy storage LIBs accurately and efficiently, a long-term SOH estimation method based on NDS-BFO algorithm and SA-BP model is proposed in this paper. Among them, the NDS-BFO algorithm is used to identify the maximum solid-phase lithium-ion concentration of the positive and negative electrodes in the SP model. Besides, the superiority and versatility of using the above-mentioned parameters as HIs are demonstrated in this paper. And this paper highlights the improvement effect of NDS-BFO algorithm by comparing the identification results and computational costs of NDS-BFO algorithm and BFO algorithm in different degradation cycles. On this basis, the above HIs are used as the input of the SA-BP model to estimate the long-term SOH during degradation. At 25 °C, under the 0.5 C constant current working condition, the RMSE, MAE and MAPE of the long-term SOH estimation of one cell are 0.42%, 0.34% and 0.38, respectively. At 25 °C, under the self-designed energy storage working condition, the RMSE, MAE and MAPE of long-term SOH estimation of another cell are 0.33%, 0.26% and 0.29, respectively. In addition, this paper also compares the existing methods and the proposed SOH estimation method through several evaluation indicators and HIs. The results indicate that the proposed method has better estimation effects. The experimental results verify the superiority of the proposed algorithm in the long-term SOH estimation. Besides, the results indicate that the proposed algorithm can meet the requirements of LIBs in the energy storage system. Future work can focus on long-term SOH estimation studies for LIB packs.

## Acknowledgments

The authors acknowledge the financial support from National Natural Science Foundation of China (No. 61801407), China Scholarship Council (No.201908515099), and Fund of Robot Technology Used for Special Environment Key Laboratory of Sichuan Province (No.18kftk03).

## References

1. Chen Xiaojiao, H.L., Liu Junbo, Song Dongran, Yang Sheng, *Peak shaving benefit assessment considering the joint operation of nuclear and battery energy storage power stations: Hainan case study*. Energy, 2022. **239**(PA): p. 1-15.
2. Ahmed Zayed AL Shaqsi, K.S., Amr Al-Hinai, *Review of energy storage services, applications, limitations, and benefits*. Energy Reports, 2020. **6**(S7): p. 288-306.
3. Olabi, A.G., *Renewable energy and energy storage systems*. Energy, 2017. **136**(10): p. 1-6.
4. Jin Yang, Z.Z., Miao Shan, Wang Qingsong, Sun Lei, Lu Hongfei, *Explosion hazards study of grid-scale lithium-ion battery energy storage station*. Journal of Energy Storage, 2021. **42**(10): p. 102987-102998.
5. Gholizadeh, M. and A. Yazdizadeh, *Systematic mixed adaptive observer and EKF approach to estimate SOC and SOH of lithium-ion battery*. IET Electrical Systems in Transportation, 2020. **10**(2): p. 1-15.
6. Fang, L., J. Li, and B. Peng, *Online Estimation and Error Analysis of both SOC and SOH of Lithium-ion Battery based on DEKF Method*. Energy Procedia, 2019. **158**(1): p. 1-10.
7. Yuanjun, G., et al., *A compact and optimized neural network approach for battery state-of-charge estimation of energy storage system*. Energy, 2021. **219**(1): p. 1-14.
8. Hu, X., et al., *Technological Developments in Batteries: A Survey of Principal Roles, Types, and Management Needs*. IEEE Power and Energy Magazine, 2017. **15**(5): p. 1-7.
9. Robert, Z., G. Pravinray, and B. Adam, *Lithium-ion energy storage battery explosion incidents*. Journal of Loss Prevention in the Process Industries, 2021. **72**(9): p. 104560-104571.
10. Jin, G., et al., *Comparison of SOC Estimation between the Integer-Order Model and Fractional-Order Model Under Different Operating Conditions*. Energies, 2020. **13**(7): p. 1785-1797.
11. Zhenhua Cui, L.K., Liwei Li, Licheng Wang, Kai Wang, *A combined state-of-charge estimation method for lithium-ion battery using an improved BGRU network and UKF*. Energy, 2022. **259**(1): p. 124933-124945.
12. Wassiliadis, N., et al., *Revisiting the dual extended Kalman filter for battery state-of-charge and state-of-health estimation: A use-case life cycle analysis*. Journal of Energy Storage, 2018. **19**(10): p. 73-87.
13. Luo, Y., et al., *State of charge estimation method based on the extended Kalman filter algorithm with consideration of time-varying battery parameters*. International Journal of Energy Research, 2020. **44**(13): p. 10538-10550.
14. Hu Xiaosong, Z.K., Liu Kailong, *Advanced Fault Diagnosis for Lithium-ion Battery Systems: a Review of Fault Mechanisms, Fault Features, and Diagnosis Procedures*. IEEE Industrial Electronics Magazine, 2020. **14**(3): p. 65-91.
15. Xu, L., Z. Deng, and X. Hu, *Battery Health Estimation Using Electrochemical Aging Model and Ensemble Kalman Filtering*. IEEE International Future Energy Electronics Conference, 2021. **1**(1): p. 1-6.
16. Xiaojun, T., et al., *Online state-of-health estimation of lithium-ion battery based on dynamic parameter identification at multi timescale and support vector regression*. Journal of Power Sources, 2021. **484**(1): p. 1-10.
17. Sun, Y., et al., *Remaining useful life prediction for lithium-ion batteries based on an integrated health indicator*. Microelectronics Reliability, 2018. **88-90**(9): p. 1189-1194.
18. Kang, B.O., et al., *Economic analysis of a customer-installed energy storage system for both self-saving operation*

- and demand response program participation in South Korea.* Renewable and Sustainable Energy Reviews, 2018. **94**(10): p. 69-83.
19. Feng, F., et al., *Propagation mechanisms and diagnosis of parameter inconsistency within Li-Ion battery packs.* Renewable and Sustainable Energy Reviews, 2019. **112**(1): p. 1-18.
  20. Ran, X., et al., *A Novel Joint Estimation Method of State of Charge and State of Health Based on the Strong Tracking-Dual Adaptive Extended Kalman Filter Algorithm for the Electric Vehicle Lithium-Ion Batteries.* International Journal of Electrochemical Science, 2021. **16**(11): p. 1-32.
  21. Zhang, S., et al., *A rapid online calculation method for state of health of lithium-ion battery based on coulomb counting method and differential voltage analysis.* Journal of Power Sources, 2020. **479**(15): p. 228740-228749.
  22. Li, X., et al., *State-of-health estimation for Li-ion batteries by combing the incremental capacity analysis method with grey relational analysis.* Journal of Power Sources, 2019. **410-411**(1): p. 1-12.
  23. Sijia, Y., et al., *Review on state-of-health of lithium-ion batteries: Characterizations, estimations and applications.* Journal of Cleaner Production, 2021. **314**(10): p. 128015-128024.
  24. Chen, D., et al., *Pomegranate-like Silicon-based anodes self-assembled by hollow-structured Si/void@C nanoparticles for Li-ion batteries with high performances.* Nanotechnology, 2020. **32**(9): p. 1-9.
  25. Xin Zhou, J.L.S., Tulga Ersal, *Battery state of health monitoring by estimation of the number of cyclable Li-ions.* Control Engineering Practice, 2017. **66**(9): p. 51-63.
  26. Prasad, G.K. and C.D. Rahn, *Model based identification of aging parameters in lithium ion batteries.* Journal of Power Sources, 2013. **232**(15): p. 79-85.
  27. Lipu, M.S.H., et al., *A review of state of health and remaining useful life estimation methods for lithium-ion battery in electric vehicles: Challenges and recommendations.* Journal of Cleaner Production, 2018. **205**(20): p. 115-133.
  28. ShunLi, W., et al., *An improved coulomb counting method based on dual open- circuit voltage and real- time evaluation of battery dischargeable capacity considering temperature and battery aging.* International Journal of Energy Research, 2021. **45**(12): p. 17609-17621.
  29. Dezhi Li, D.Y., Liwei Li, Licheng Wang, Kai Wang, *Electrochemical Impedance Spectroscopy Based on the State of Health Estimation for Lithium-Ion Batteries.* Energies, 2022. **15**(18): p. 6665-6674.
  30. Li, S.E., et al., *An electrochemistry-based impedance model for lithium-ion batteries.* Journal of Power Sources, 2014. **258**(1): p. 9-18.
  31. Westerhoff, U., et al., *Electrochemical impedance spectroscopy based estimation of the state of charge of lithium-ion batteries.* Journal of Energy Storage, 2016. **8**(9): p. 244-256.
  32. Yoon, S., et al., *Power capability analysis in lithium ion batteries using electrochemical impedance spectroscopy.* Journal of Electroanalytical Chemistry, 2011. **655**(1): p. 32-38.
  33. Chiang, Y.-H., W.-Y. Sean, and J.-C. Ke, *Online estimation of internal resistance and open-circuit voltage of lithium-ion batteries in electric vehicles.* Journal of Power Sources, 2011. **196**(8): p. 3921-3932.
  34. Xiong, R., L. Li, and J. Tian, *Towards a smarter battery management system: A critical review on battery state of health monitoring methods.* Journal of Power Sources, 2018. **405**(30): p. 18-29.
  35. Wei, Z., et al., *Probing Li-ion concentration in an operating lithium ion battery using in situ Raman spectroscopy.* Journal of Power Sources, 2020. **449**(15): p. 227361-227370.
  36. Shuzhi, Z., et al., *Synchronous estimation of state of health and remaining useful lifetime for lithium-ion battery using the incremental capacity and artificial neural networks.* Journal of Energy Storage, 2019. **26**(12): p. 100951-100961.
  37. Eddahech, A., et al., *Behavior and state-of-health monitoring of Li-ion batteries using impedance spectroscopy and recurrent neural networks.* International Journal of Electrical Power and Energy Systems, 2012. **42**(1): p. 487-494.
  38. You, G.-w., S. Park, and D. Oh, *Real-time state-of-health estimation for electric vehicle batteries: A data-driven approach.* Applied Energy, 2016. **176**(15): p. 92-103.
  39. Zhenhua Cui, L.K., Liwei Li, Licheng Wang, Kai Wang, *A hybrid neural network model with improved input for*

- state of charge estimation of lithium-ion battery at low temperatures*. Renewable Energy, 2022. **98**(1): p. 1328-1340.
40. Xin, S., et al., *A review of non-probabilistic machine learning-based state of health estimation techniques for Lithium-ion battery*. Applied Energy, 2021. **300**(15): p. 117346-117357.
  41. Yang, D., et al., *A Neural Network Based State-of-Health Estimation of Lithium-ion Battery in Electric Vehicles*. Energy Procedia, 2017. **105**(5): p. 2059-2064.
  42. Lucian Ungurean, M.V.M., Gabriel Cârstoiu, *Online state of health prediction method for lithium-ion batteries, based on gated recurrent unit neural networks*. International Journal of Energy Research, 2020. **44**(8): p. 6767-6777.
  43. Khumprom, P. and N. Yodo, *A Data-Driven Predictive Prognostic Model for Lithium-ion Batteries based on a Deep Learning Algorithm*. Energies, 2019. **12**(4): p. 660-669.
  44. Chunli Liu, D.L., Licheng Wang, Liwei Li, Kai Wang, *Strong Robustness and High Accuracy Remaining Useful Life Prediction on Supercapacitors*. APL Materials, 2022. **10**(6): p. 061106-061117.
  45. Pan, H., et al., *Novel battery state-of-health online estimation method using multiple health indicators and an extreme learning machine*. Energy, 2018. **160**(1): p. 466-477.
  46. Zheng Chen, Q.X.Y.L., Jiangwei Sshen, Renxin Xiao, *State of Health Estimation for Lithium-Ion Batteries Based on Elman Neural Network*. DEStech Transactions on Environment Energy and Earth Science, 2019. **1**(1): p. 1-10.
  47. Lee JongHyun, L.I., *Lithium Battery SOH Monitoring and an SOC Estimation Algorithm Based on the SOH Result*. Energies, 2021. **14**(15): p. 1-14.
  48. Shen, S., et al., *A deep learning method for online capacity estimation of lithium-ion batteries*. Journal of Energy Storage, 2019. **25**(10): p. 100817-100825.
  49. Jong-Hyun Lee, H.-S.K., In-Soo Lee, *Deep Neural Network based SOH Monitoring of Battery module*. 2019 IEEE Eurasia Conference on IOT, Communication and Engineering (ECICE), 2019. **1**(1): p. 1-7.
  50. Hannan, M.A., et al., *A review of lithium-ion battery state of charge estimation and management system in electric vehicle applications: Challenges and recommendations*. Renewable and Sustainable Energy Reviews, 2017. **78**(10): p. 834-854.
  51. Nuhic, A., et al., *Health diagnosis and remaining useful life prognostics of lithium-ion batteries using data-driven methods*. Journal of Power Sources, 2013. **239**(1): p. 680-688.
  52. Liu, Z., et al., *A New Lithium-Ion Battery SOH Estimation Method Based on an Indirect Enhanced Health Indicator and Support Vector Regression in PHMs*. Energies, 2020. **13**(4): p. 1-14.
  53. Wang, D., Q. Miao, and M. Pecht, *Prognostics of lithium-ion batteries based on relevance vectors and a conditional three-parameter capacity degradation model*. Journal of Power Sources, 2013. **239**(1): p. 253-264.
  54. Li, H., D. Pan, and C.L.P. Chen, *Intelligent Prognostics for Battery Health Monitoring Using the Mean Entropy and Relevance Vector Machine*. IEEE Trans. Systems, Man, and Cybernetics: Systems, 2014. **44**(7): p. 851-862.
  55. Yajun, Z., et al., *State-of-health estimation for lithium-ion batteries by combining model-based incremental capacity analysis with support vector regression*. Energy, 2022. **239**(15): p. 121986-121995.
  56. M., M., et al., *Lithium-ion battery SoH estimation based on incremental capacity peak tracking at several current levels for online application*. Microelectronics Reliability, 2020. **114**(11): p. 113798-113805.
  57. Arunava, N., et al., *An Incremental Voltage Difference Based Technique for Online State of Health Estimation of Li-ion Batteries*. Scientific reports, 2020. **10**(1): p. 9526-9534.
  58. Yanxin, X., et al., *Improved gray wolf particle filtering and high- fidelity second- order autoregressive equivalent modeling for intelligent state of charge prediction of lithium- ion batteries*. International Journal of Energy Research, 2021. **45**(13): p. 19203-19214.
  59. Cong, J., et al., *A state-of-charge estimation method of the power lithium-ion battery in complex conditions based on adaptive square root extended Kalman filter*. Energy, 2021. **219**(15): p. 119603-119624.
  60. Zeng, M., et al., *SOC and SOH Joint Estimation of the Power Batteries Based on Fuzzy Unscented Kalman Filtering Algorithm*. Energies, 2019. **12**(16): p. 3122-3131.
  61. He, Y., et al., *Equivalent hysteresis model based SOC estimation with variable parameters considering temperature*.

- Journal of Power Electronics, 2021. **21**(3): p. 590-602.
62. Hu, X., S. Li, and H. Peng, *A comparative study of equivalent circuit models for Li-ion batteries*. Journal of Power Sources, 2011. **198**(15): p. 359-367.
  63. Tian, H., et al., *A review of the state of health for lithium-ion batteries: Research status and suggestions*. Journal of Cleaner Production, 2020. **261**(10): p. 120813-120821.
  64. Feng, G.M., et al., *A review on state of health estimations and remaining useful life prognostics of lithium-ion batteries*. Measurement, 2021. **174**(4): p. 109057-109064.
  65. E. Rijanto, L.R., A. Nugroho and S. Kanarachos, *RLS with optimum multiple adaptive forgetting factors for SoC and SoH estimation of Li-Ion battery*. 2017 5th International Conference on Instrumentation, Control, and Automation (ICA), 2017. **1**(1): p. 73-77.
  66. Jinjin, S., G. Haisheng, and C. Dewang, *Parameter identification method for lithium-ion batteries based on recursive least square with sliding window difference forgetting factor*. Journal of Energy Storage, 2021. **44**(15): p. 103485-103494.
  67. Li, X., Z. Wang, and L. Zhang, *Co-estimation of capacity and state-of-charge for lithium-ion batteries in electric vehicles*. Energy, 2019. **174**(1): p. 33-44.
  68. Rui, X., et al., *A Double-Scale, Particle-Filtering, Energy State Prediction Algorithm for Lithium-Ion Batteries*. IEEE Transactions on Industrial Electronics, 2018. **65**(2): p. 1526-1538.
  69. Liuyi, L. and W. Ying, *State-of-Charge and State-of-Health Estimation for Lithium-Ion Batteries Based on Dual Fractional-Order Extended Kalman Filter and Online Parameter Identification*. IEEE ACCESS, 2021. **9**(1): p. 1-12.
  70. Lili, M., et al., *Co-estimation of state of charge and state of health for lithium-ion batteries based on fractional-order model with multi-innovations unscented Kalman filter method*. Journal of Energy Storage, 2022. **52**(15): p. 104904-104912.
  71. Bi, J., et al., *State-of-health estimation of lithium-ion battery packs in electric vehicles based on genetic resampling particle filter*. Applied Energy, 2016. **182**(15): p. 558-568.
  72. Deng, Z., et al., *Polynomial approximation pseudo-two-dimensional battery model for online application in embedded battery management system*. Energy, 2018. **142**(1): p. 838-850.
  73. Lee, J.L., A. Chemistruck, and G.L. Plett, *One-dimensional physics-based reduced-order model of lithium-ion dynamics*. Journal of Power Sources, 2012. **220**(15): p. 430-448.
  74. Lichao, R., et al., *An algorithm for state of charge estimation based on a single-particle model*. Journal of Energy Storage, 2021. **39**(7): p. 102644-102651.
  75. T. R. B. Grandjean, L.L., M. X. Odio and W. D. Widanage, *Global Sensitivity Analysis of the Single Particle Lithium-Ion Battery Model with Electrolyte*. 2019 IEEE Vehicle Power and Propulsion Conference (VPPC), 2019. **1**(1): p. 1-7.
  76. Rohit, M. and G. Amit, *An improved single-particle model with electrolyte dynamics for high current applications of lithium-ion cells*. Electrochimica Acta, 2021. **389**(1): p. 138623-138631.
  77. Ma, et al., *Establishment and simulation of an electrode averaged model for a lithium-ion battery based on kinetic reactions*. RSC Advances, 2016. **6**(30): p. 1-14.
  78. Zhuoyan Wu, L.Y., Ran Xiong., Shunli Wang, Wei Xiao, Yi Liu, Jun Jia, Yanchao Liu, *A Novel State of Health Estimation of Lithium-ion Battery Energy Storage System Based on Linear Decreasing Weight-Particle Swarm Optimization Algorithm and Incremental Capacity-Differential Voltage Method*. International Journal of Electrochemical Science, 2022. **17**(7): p. 1-32.
  79. Moura, S.J., M. Krstic, and N.A. Chaturvedi, *Adaptive PDE Observer for Battery SOC/SOH Estimation*. ASME 2012 5th Annual Dynamic Systems and Control Conference joint with the JSME 2012 11th Motion and Vibration Conference, 2012. **1**(9): p. 101-110.
  80. Xiong, R., et al., *A systematic model-based degradation behavior recognition and health monitoring method for*

- lithium-ion batteries*. Applied Energy, 2017. **207**(1): p. 372-383.
81. A. Zenati, P.D.a.H.R., *Estimation of the SOC and the SOH of li-ion batteries, by combining impedance measurements with the fuzzy logic inference*. IECON 2010 - 36th Annual Conference on IEEE Industrial Electronics Society, 2010. **1**(1): p. 1773-1778.
  82. Che Yanbo, C.Y., Li Hongfeng, Liu Yushu, Jiang Mingda, Qin Peijun, *SOH estimation method for lithium-ion batteries based on nonlinear autoregressive neural network model with exogenous input*. Journal of Electrochemical Energy Conversion and Storage, 2021. **1**(1): p. 1-28.
  83. Jinhyeong Park, M.L., Gunwoo Kim, Seongyun Park, Jonghoon Kim, *Integrated Approach Based on Dual Extended Kalman Filter and Multivariate Autoregressive Model for Predicting Battery Capacity Using Health Indicator and SOC/SOH*. Energies, 2020. **13**(9): p. 2138-2150.
  84. Chu, Z., et al., *A control-oriented electrochemical model for lithium-ion battery, Part I: Lumped-parameter reduced-order model with constant phase element*. Journal of Energy Storage, 2019. **25**(10): p. 100828-100839.
  85. Yaxiang Fan, F.X., Chaoran Li, Guorun Yang, Xin Tang, *A novel deep learning framework for state of health estimation of lithium-ion battery*. Journal of Energy Storage, 2020. **32**(12): p. 101741-101751.
  86. Kirandeep Kaur, A.G., Xujian Cui, Surinder Singh, Bijaya Ketan Panigrahi, *Deep learning networks for capacity estimation for monitoring SOH of Li-ion batteries for electric vehicles*. International Journal of Energy Research, 2021. **45**(2): p. 3113-3128.
  87. Yang Li, J.T., *CNN and transfer learning based online SOH estimation for lithium-ion battery*. 2020 Chinese Control And Decision Conference (CCDC), 2020. **1**(1): p. 19872038-19872045.
  88. Xin Sui, S.H., Søren B. Vilsen, Jinhao Meng, Remus Teodorescu, Daniel-Ioan Stroe, *A review of non-probabilistic machine learning-based state of health estimation techniques for Lithium-ion battery*. Applied Energy, 2021. **300**(15): p. 117346-117354.
  89. Dongdong, G., et al., *Extreme Learning Machine Using Bat Optimization Algorithm for Estimating State of Health of Lithium-Ion Batteries*. Applied Sciences, 2022. **12**(3): p. 1398-1407.
  90. Kaiquan, L., W. Yujie, and C. Zonghai, *A comparative study of battery state-of-health estimation based on empirical mode decomposition and neural network*. Journal of Energy Storage, 2022. **54**(10): p. 105333-105348.
  91. Chang, C., Wang, S., Jiang, J., Gao, Y., Jiang, Y., and Liao, L, *Lithium-Ion Battery State of Health Estimation Based on Electrochemical Impedance Spectroscopy and Cuckoo Search Algorithm Optimized Elman Neural Network*. Journal of Electrochemical Energy Conversion and Storage, 2022. **19**(3): p. 030912-030922.
  92. Zheng, C., et al., *State of health estimation for lithium-ion batteries based on temperature prediction and gated recurrent unit neural network*. Journal of Power Sources, 2022. **521**(15): p. 230892-230904.